

## Nonlinear flow generation by electrostatic turbulence in tokamaks

W. X. Wang,<sup>1,a)</sup> P. H. Diamond,<sup>2</sup> T. S. Hahm,<sup>1</sup> S. Ethier,<sup>1</sup> G. Rewoldt,<sup>1</sup> and W. M. Tang<sup>1</sup>

<sup>1</sup>Plasma Physics Laboratory, Princeton University, P.O. Box 451,  
Princeton, New Jersey 08543, USA

<sup>2</sup>University of California, San Diego, La Jolla, California 92093, USA

(Received 6 April 2010; accepted 11 June 2010; published online 22 July 2010)

Global gyrokinetic simulations have revealed an important nonlinear flow generation process due to the residual stress produced by electrostatic turbulence of ion temperature gradient (ITG) modes and trapped electron modes (TEMs). In collisionless TEM (CTEM) turbulence, nonlinear residual stress generation by both the fluctuation intensity and the intensity gradient in the presence of broken symmetry in the parallel wavenumber spectrum is identified for the first time. Concerning the origin of the symmetry breaking, turbulence self-generated low frequency zonal flow shear has been identified to be a key, universal mechanism in various turbulence regimes. Simulations reported here also indicate the existence of other mechanisms beyond  $\mathbf{E} \times \mathbf{B}$  shear. The ITG turbulence driven “intrinsic” torque associated with residual stress is shown to increase close to linearly with the ion temperature gradient, in qualitative agreement with experimental observations in various devices. In CTEM dominated regimes, a net toroidal rotation is driven in the cocurrent direction by intrinsic torque, consistent with the experimental trend of observed intrinsic rotation. The finding of a “flow pinch” in CTEM turbulence may offer an interesting new insight into the underlying dynamics governing the radial penetration of modulated flows in perturbation experiments. Finally, simulations also reveal highly distinct phase space structures between CTEM and ITG turbulence driven momentum, energy, and particle fluxes, elucidating the roles of resonant and non-resonant particles. © 2010 American Institute of Physics. [doi:10.1063/1.3459096]

### I. INTRODUCTION

Momentum transport and plasma flow generation are complex transport phenomena of great importance in magnetic confinement fusion. An optimized plasma flow is believed to play a critical role in both controlling large scale (macroscopic) plasma stability and in reducing energy loss due to plasma microturbulence and thereby achieving high quality performance in plasma confinement. The toroidal momentum transport has been observed to be highly anomalous in various magnetic fusion experiments not only for its high level compared to the neoclassical value due to Coulomb collisions<sup>1</sup> but also for its highly pronounced non-diffusive and nonlocal nature. A striking finding is the observation of automatic toroidal rotation spin up in nearly all tokamaks, the so called intrinsic or spontaneous rotation,<sup>2–4</sup> i.e., toroidal plasmas can self-organize and develop rotation without an external momentum input. Nondiffusive phenomena can also exist in other transport channels such as energy and particle; however, evidences so far in experiments appear not as intriguing as the intrinsic rotation. This phenomenon may play a critical role in determining plasma flows and, consequently, confinement performance, particularly in the International Thermonuclear Experimental Reactor. Note that intrinsic rotation in tokamaks is an example of a “negative viscosity phenomenon” in which an up-gradient component of the momentum flux organizes a structured mean flow. Negative viscosity phenomena are of broad interest in the

context of atmospheres, oceans, stellar interiors, and other rotating fluids.

Understanding the momentum transport and flow generation is one of the highlighted issues of current fusion research. Out of various possible physical mechanisms governing plasma flow dynamics, the strong coupling between toroidal momentum and energy transport universally observed in fusion experiments suggests that microturbulence is a key player in determining plasma rotation as well. The strong momentum-energy transport coupling via microturbulence as a “medium” was predicted by theory<sup>5</sup> and observed in experiments<sup>6</sup> about two decades ago. The strong coupling was also obtained by gyrokinetic simulations of ion temperature gradient (ITG) turbulence over a wide range of plasma parameters.<sup>7</sup>

For turbulence driven toroidal momentum flux, a generic structure can be expressed as follows:

$$\Gamma_{\phi} \propto -\chi_{\phi} \frac{\partial U_{\phi}}{\partial r} + V_p U_{\phi} + \Pi_{r,\phi}^{\text{rs}}.$$

In addition to diffusion (first term), there are two nondiffusive components, momentum pinch (second term) and residual stress (third term). The three components in the momentum flux are highly distinctive not only formally but also physically. Besides their different physical origins under turbulence circumstances, they have qualitatively distinct effects on the toroidal flow formation. The diffusive transport is well known in the direction opposite to the rotation gradient, leading to the relaxation of the rotation profile and the release of associated free energy. The momentum pinch term

<sup>a)</sup>Electronic mail: wwang@pppl.gov.

is a convective flux, which is directly proportional to the rotation velocity  $U_\phi$  with  $V_p$  as the pinch velocity. Both momentum diffusion and pinch can move plasma mechanical momentum (i.e., toroidal momentum carried by particles) and then rearrange the rotation profile radially. A qualitative distinction is that momentum pinch can transport momentum in either direction, up-gradient or down-gradient.

The residual stress is defined as a specific part of the Reynolds stress, which depends directly on neither the rotation velocity nor its gradient. The residual stress has a fundamentally distinct effect on rotation profiles and is shown to drive intrinsic rotation as a type of wave-driven flow phenomenon, which operates via wave-particle momentum exchange.<sup>8</sup> Obviously, it has no counterpart in the turbulence driven particle flux, which, under the constraint of particle number conservation, consists of only diffusive (including sub- and superdiffusive) and convective components. On the other hand, the energy flux may contain a residual-stress-like component due to energy exchange between particles and waves. The residual stress  $\Pi_{r,\phi}^{\text{rs}}$  can be shown in the momentum transport equation to be isomorphic in mathematical form to the integrated external momentum source,<sup>9</sup> which acts as a torque to drive the rotation. Thus, the residual stress can act as an internal local torque to spin up a plasma, offering an ideal mechanism to drive intrinsic rotation. For this reason, the quantity  $\nabla \cdot \Pi_{r,\phi}^{\text{rs}}$  is widely referred to as the intrinsic torque in experimental and theoretical investigations. Note that all three components have been observed in tokamak experiments. Searching for nondiffusive elements and understanding underlying mechanisms have been the focus of recent intensive theoretical and experimental efforts.

In this paper, new results of nondiffusive toroidal momentum transport found from our global gyrokinetic simulations are reported. We focus our study on understanding the nonlinear residual stress generation and its effect on toroidal flow formation in electrostatic turbulence regimes of ITG modes and trapped electron modes (TEMs). This study concerns a few critical issues, which are highly relevant to experimental observations and theoretical studies. These include (i) mechanisms for turbulence driving residual stress, (ii) mechanisms for breaking symmetry in the parallel wavenumber  $k_\parallel$  spectrum [the symmetry breaking is shown to be a critical ingredient for turbulence to generate net acceleration of parallel (and toroidal) flows<sup>9-15</sup>], (iii) impacts of trapped electrons and electron turbulence on residual stress, (iv) characteristic dependences of intrinsic rotation on plasma parameters and directional tendency of the rotation, and (vi) the fraction of residual stress in the momentum flux. Remarkable results also include the finding of an interesting mesoscale phenomenon, “flow pinch,” in collisionless TEM (CTEM) turbulence, which appears to phenomenologically reproduce the radial penetration of modulated flows demonstrated by perturbation experiments.<sup>16</sup> Also presented are highly distinct phase space structures between TEM and ITG turbulence driven fluxes to elucidate the roles of resonant and nonresonant particles.

The remainder of this paper is organized as follows. In Sec. II, gyrokinetic simulation models employed in this work are described, and a benchmark study of a CTEM case is

presented. In Sec. III, we discuss generic pictures of turbulence driven toroidal momentum flux obtained in our global simulations. We attempt to partition the momentum flux and calculate the fraction due to residual stress. We also examine the relationship between the momentum and the energy transport, calculating the intrinsic Prandtl number. In Sec. IV, we address the mechanism of nonlinear residual generation in ITG turbulence with focus on the effect of zonal flow shear on  $k_\parallel$  symmetry breaking. The parametric dependence of ITG driven intrinsic torque on the ion temperature gradient is explored in order to understand empirical trends observed in experiments. The key results of nonlinear residual stress and flow generation in CTEM turbulence and trapped electron effects in the ITG regime are presented in Sec. V. The role of both the turbulence intensity and the intensity gradient in driving residual stress is explored. Also discussed are highlighted mesoscale phenomena, particularly the flow pinch effect, in CTEM dominated regimes. In Sec. VI, the phase structures of momentum, energy, and particle fluxes are presented with a lot of interesting details with regard to which and how particles contribute to plasma transport due to turbulence. Section VII presents the conclusions.

## II. GYROKINETIC SIMULATION MODELS OF ROTATING PLASMA AND TREATMENT OF KINETIC ELECTRONS

In this work, our global turbulence simulation is carried out using the GYROKINETIC TOKAMAK SIMULATION (GTS) code.<sup>17</sup> The GTS code is based on a generalized gyrokinetic simulation model using a  $\delta f$  particle-in-cell approach and incorporates the comprehensive influence of noncircular cross section, realistic plasma profiles, plasma rotation, neoclassical (equilibrium) electric field, Coulomb collisions, and other features. It can directly read plasma profiles of temperature, density, and toroidal angular velocity, from the TRANSP (Ref. 18) experimental database, and a numerical magnetohydrodynamic (MHD) equilibrium reconstructed by MHD codes using TRANSP radial profiles of the total pressure and the parallel current (or safety factor), along with the plasma boundary shape.

First, we give a brief description on our gyrokinetic simulation model for rotating plasmas in this section. In a  $\delta f$  simulation, the turbulence fluctuations are considered as perturbations on top of the neoclassical equilibrium. The gyrokinetic particle distribution function is expressed as  $f=f_0+\delta f$ . The equilibrium distribution function  $f_0$  of ions, with magnetic moment  $\mu$  and parallel velocity  $v_\parallel$  as independent velocity variables, is determined by the neoclassical dynamics and obeys

$$\begin{aligned} \frac{\partial f_0}{\partial t} + (v_\parallel \hat{b} + \mathbf{v}_{E_0} + \mathbf{v}_d) \cdot \nabla f_0 - \hat{\mathbf{b}}^* \cdot \nabla \left( \mu B + \frac{e}{m_i} \Phi_0 \right) \frac{\partial f_0}{\partial v_\parallel} \\ = C_i(f_0, f_0). \end{aligned} \quad (1)$$

Here,  $\mathbf{v}_{E_0}$  is the magnetic drift velocity corresponding to the equilibrium potential  $\Phi_0$ ,  $\mathbf{v}_d$  is the  $\nabla B$  drift velocity,

$\hat{\mathbf{b}}^* = \hat{\mathbf{b}} + \rho_{\parallel} \hat{\mathbf{b}} \times (\hat{\mathbf{b}} \cdot \nabla \hat{\mathbf{b}})$ , with  $\hat{\mathbf{b}} = \mathbf{B}/B$ ,  $C_i$  is the Coulomb collision operator, and  $e$  and  $m_i$  are the ion charge and mass, respectively. The lowest order solution of Eq. (1) is a shifted Maxwellian consistent with (large) plasma rotation,<sup>19</sup>

$$f_0 = f_{SM} = n(r, \theta) \left( \frac{m_i}{2\pi T_i} \right)^{3/2} e^{-m_i/T_i [1/2(v_{\parallel} - U_i)^2 + \mu B]}, \quad (2)$$

where the parallel flow velocity  $U_i$  is associated with the toroidal rotation by  $U_i = I\omega_{\phi}/B$ , with  $\omega_{\phi}$  being the toroidal angular velocity and  $I$  the toroidal current, and  $n_i(r, \theta)$  is the ion density,  $n_i(r, \theta) = N(r) e^{m_i U_i^2 / 2T_i - e\tilde{\Phi}_0 / T_i}$ , with poloidal variation associated with plasma rotation.<sup>1</sup> The total equilibrium potential consists of two parts,  $\Phi_0 = \langle \Phi_0 \rangle + \tilde{\Phi}_0$ . Here,  $\langle \rangle$  denotes a flux-surface average. The poloidally varying compo-

nent  $\tilde{\Phi}_0$  can be generated by the centrifugal force, which drives charge separation on a magnetic surface in strongly rotating plasmas.<sup>1</sup> Generally the radial potential  $\langle \Phi_0 \rangle$  is dominant. The equilibrium radial electric field can be calculated from a first-principles based particle simulation of neoclassical dynamics with important finite orbit effects<sup>19</sup> or obtained by direct experimental measurement if available. Instead of using a true neoclassical equilibrium distribution function, which is unknown analytically, we use this lowest order solution for equilibrium toroidal plasmas in the present simulations. A shifted Maxwellian with either model or experimental profiles of  $\langle n(r, \theta) \rangle$ ,  $T_i(r)$ , and  $\omega_{\phi}(r)$  is prescribed for the ions. In the electrostatic limit, the ion gyrokinetic equation for the turbulence perturbed distribution  $\delta f_i$  of ion guiding centers is

$$\begin{aligned} \frac{\partial \delta f_i}{\partial t} + (v_{\parallel} \hat{\mathbf{b}} + \mathbf{v}_{E_0} + \mathbf{v}_E + \mathbf{v}_d) \cdot \nabla \delta f_i - \hat{\mathbf{b}}^* \cdot \nabla \left( \mu B + \frac{e}{m_i} \Phi_0 + \frac{e}{m_i} \tilde{\Phi} \right) \frac{\partial \delta f_i}{\partial v_{\parallel}} = & \left( - \left\{ \frac{m}{T_i} \left[ \frac{1}{2} (v_{\parallel} - U_i)^2 + \mu B \right] - \frac{3}{2} \right\} \mathbf{v}_E \cdot \nabla \ln T \right. \\ & \left. - \mathbf{v}_E \cdot \nabla \ln n(r, \theta) - \frac{m(v_{\parallel} - U_i)}{T_i} \mathbf{v}_E \cdot \nabla U_i(r, \theta) + \frac{mU_i}{T_i v_{\parallel}} \mathbf{v}_E \cdot \mu \nabla B - \frac{1}{T_i} (v_{\parallel} \hat{\mathbf{b}} + \mathbf{v}_d) \cdot \nabla (e\tilde{\Phi}) \left( 1 - \frac{U_i}{v_{\parallel}} \right) \right) f_0 + C_i^l(\delta f_i). \end{aligned} \quad (3)$$

Here,  $\mathbf{v}_E$  is the  $\mathbf{E} \times \mathbf{B}$  velocity corresponding to the fluctuation potential  $\tilde{\Phi}(\mathbf{R})$  at the ion guiding center coordinates  $\mathbf{R}$ , and  $C_i^l$  is the linearized Coulomb collision operator. On the right hand side, the third term proportional to  $\nabla U_i$  is the Kelvin–Helmholtz-type drive term. The other terms containing  $U_i$  are also retained, which can be important when the Mach number of plasma flow is high.

The GTS code solves the gyrokinetic Poisson equation in configuration space for the turbulence potential  $\Phi(\mathbf{x})$  at the particle coordinates  $\mathbf{x}$ . Unlike in flux-tube or wedge codes, the real space, global Poisson solver, in principle, retains all toroidal modes from  $(m/n=0/0)$  all the way to a limit that is set by grid resolution and therefore retains full-channel nonlinear energy couplings. There are two largely different Poisson solvers implemented in the GTS simulation. In a simple geometry limit, i.e., large aspect ratio and circular cross section, turbulence fluctuations  $\delta\Phi$  on small spatial and fast time scales and axisymmetric zonal flow  $\langle \Phi \rangle$  on larger (mesoscale) spatial and slow time scales can be decoupled using (i) a Pade approximation, i.e.,  $\Gamma_0(b) \equiv I_0(b)e^{-b} \approx 1/(1+b)$ , with  $I_0$  being the modified Bessel function and  $b = (k_{\perp} \rho_i)^2$ , and (ii)  $\langle \tilde{\Phi} \rangle \approx \langle \Phi \rangle$ , i.e., operations between the flux-surface average  $\langle \Phi \rangle$  and the gyrokinetic double average  $\tilde{\Phi}$  can commute. This results in two decoupled equations,<sup>17</sup>

$$\frac{e}{T_i} (\delta\Phi - \tilde{\Phi}) = \frac{\delta\bar{n}_i - \langle \delta\bar{n}_i \rangle}{n_0} - \frac{\delta n_e - \langle \delta n_e \rangle}{n_0}, \quad (4)$$

$$\begin{aligned} & \frac{1}{\mathcal{V}'_r} \frac{d}{dr} \left[ \frac{d\langle \Phi \rangle}{dr} \mathcal{V}'_r \langle g^{rr} \rangle \right] \\ & = \frac{1}{\mathcal{V}'_r} \frac{d}{dr} \left\{ \frac{d}{dr} \left[ \frac{T_i}{e} \left( \frac{\langle \delta\bar{n}_i \rangle}{n_0} - \frac{\langle \delta n_e \rangle}{n_0} \right) \right] \mathcal{V}'_r \langle g^{rr} \rangle \right\} \\ & \quad - \left\langle \frac{1}{\rho_i^2} \right\rangle \frac{T_i}{e} \left( \frac{\langle \delta\bar{n}_i \rangle}{n_0} - \frac{\langle \delta n_e \rangle}{n_0} \right), \end{aligned} \quad (5)$$

where  $\delta\bar{n}_i(\mathbf{x})$  and  $\delta n_e(\mathbf{x})$  are the ion and electron density fluctuations, respectively,  $\mathcal{V}'_r \equiv d\mathcal{V}/dr$ , with  $\mathcal{V}$  being the volume enclosed by magnetic surface  $r$ , and  $g^{rr} \equiv \nabla r \cdot \nabla r$ . Because turbulence dynamics on different spatiotemporal scales is separated in solving the Poisson equation, the advantages are apparent. However, the above approximations, particularly the second one, are not well justified in general toroidal geometry. This has motivated us to develop a generalized Poisson solver, which solves an integral equation for the total potential  $\Phi = \delta\Phi + \langle \Phi \rangle$ ,

$$\frac{e}{T_i} (\Phi - \tilde{\Phi}) = \frac{\delta\bar{n}_i}{n_0} - \frac{\delta n_e}{n_0}. \quad (6)$$

While the adiabatic electron model has been widely used for simplicity in many earlier numerical and theoretical studies of ITG driven turbulence, nonadiabatic electron physics is in general irreducible in turbulence dynamics of toroidal systems. For ITG and TEM turbulence with  $k_{\perp} \rho_e \ll 1$ , we use a drift kinetic description for electrons, neglecting the finite gyroradius effect. However, for electron gyroradius scale turbulence, such as electron temperature gradient driven turbulence, electrons are treated as fully gyrokinetic. Similarly for

ions, the  $\delta f$  method can be used to solve for the total perturbed electron guiding center distribution function,  $\delta f_e = f_e - f_{e0}$ , corresponding to turbulence fluctuations. The equilibrium distribution  $f_{e0}$  satisfies the electron version of Eq. (1) and can be approximated by a shifted Maxwellian containing a parallel flow similar to that for the ions. Apparently,  $\delta f_e$  contains both adiabatic and nonadiabatic electron response. Another simulation model to treat kinetic electrons is to separate the nonadiabatic electron response  $\delta h_e$  using  $f_e = f_{e0} + (e\delta\Phi/T_e)f_{e0} + \delta h_e$  and to solve for the nonadiabatic part  $\delta h_e$  according to Eq. (16) in Ref. 17. In this case, Eq. (4) becomes

$$\left(1 + \frac{T_i}{T_e}\right) \frac{e\delta\Phi}{T_i} - \frac{e\widetilde{\delta\Phi}}{T_i} = \frac{\widetilde{\delta n_i} - \langle \delta n_i \rangle}{n_0} - \frac{\delta n_e^h - \langle \delta n_e^h \rangle}{n_0}, \quad (7)$$

and Eq. (6) becomes

$$\left(1 + \frac{T_i}{T_e}\right) \frac{e\Phi}{T_i} - \frac{e\widetilde{\Phi}}{T_i} - \frac{e\langle \Phi \rangle}{T_e} = \frac{\delta n_i}{n_0} - \frac{\delta n_e^h}{n_0}, \quad (8)$$

where  $\delta n_e^h \equiv \int d^3v \delta h_e$  is the nonadiabatic electron density fluctuation.

The left-hand side of the  $\delta h_e$  equation [Eq. (16) in Ref. 17] contains a time derivative term,  $\partial\delta\Phi/\partial t$ , which can easily give rise to numerical instability if it is calculated using direct finite differences. To avoid the numerical problem, a split-weight scheme<sup>20</sup> was proposed, which uses a separate equation for calculating  $\partial\Phi/\partial t$ . The  $\partial\Phi/\partial t$  equation, which is not a new equation, is obtained by taking the time derivative of the gyrokinetic Poisson equation and using the ion and electron continuity equations. In a toroidal system, the equation for calculating  $\partial\Phi/\partial t$  is obtained as follows:

$$\frac{e}{T_i} \left( \frac{\partial\Phi}{\partial t} - \frac{\widetilde{\partial\Phi}}{\partial t} \right) = \frac{1}{n_0} (\nabla \cdot \Gamma_e - \nabla \cdot \Gamma_i) + \frac{c\mathbf{B} \times \nabla\delta\Phi}{B^2} \cdot \left( 2\frac{\nabla B}{B} - \frac{e}{T_e} \nabla\Phi_0 \right), \quad (9)$$

where the wide-tilde denotes the gyrokinetic double average over  $\partial\Phi/\partial t$ , electron particle flux  $\Gamma_e \equiv \int d^3v (v_{\parallel}\mathbf{b} + \mathbf{v}_{E_0} + \mathbf{v}_E + \mathbf{v}_d)\delta h_e$ , and ion particle flux  $\Gamma_i \equiv (1/2\pi) \int d^3v d\mathbf{R} d\Theta (v_{\parallel}\mathbf{b} + \mathbf{v}_{E_0} + \mathbf{v}_E + \mathbf{v}_d)\delta f_i \delta(\mathbf{R} - \mathbf{x} + \rho)$ , with  $\rho$  being the gyroradius vector and  $\Theta$  being the gyrophase. Then  $\partial\delta\Phi/\partial t$  is calculated directly using  $\partial\delta\Phi/\partial t \equiv \delta\Phi/\partial t - \langle \delta\Phi/\partial t \rangle$ .

It is noticed that many previous simulations include only trapped electrons for the nonadiabatic electron response. Numerically, the fast parallel streaming of passing electrons gives rise to a strict constraint on the time step size, which adds to the computational challenge. While the trapped electrons are the primary origin of nonadiabatic response, some passing electrons can be nonadiabatic too. In fact, dynamical division between trapped and passing electrons is, though not impossible, highly nontrivial during simulations because of the dependence of the trapping-passing boundary on the electric potential, which evolves in time, and of the collisional trapping-detraping process. Nevertheless, thanks to

the availability of supercomputing capabilities, we retain full electron dynamics by including both trapped and untrapped electrons in the simulations.

The GTS simulation has been benchmarked against other gyrokinetic codes in the electrostatic regime and the large aspect ratio circular concentric geometry limit. Presented here are benchmark results of the trapped electron mode instability against the FULL code.<sup>21</sup> The FULL code is a linear eigenvalue code, which calculates linear growth rates and real frequencies; it is radially local (corresponding to flux tube geometry), using the so-called ballooning representation. For this benchmark, an analytical equilibrium based on the so-called “ $s-\alpha$ ” model with  $\alpha=0$  is used in the FULL local calculations, and a corresponding numerical equilibrium is produced for GTS. The numerical equilibrium includes a small Shafranov shift due to nonzero plasma beta and higher order (in the small inverse aspect ratio) corrections, which are neglected in the analytical equilibrium. The representative parameters used in the benchmark are inverse aspect ratio  $a/R_0=0.35$ , density and electron temperature profiles  $R_0/L_n=R_0/L_{T_e}=6.0 \exp\{-(r-0.5)/0.28\}^6$ , ion temperature profiles  $R_0/L_{T_i}=1.0 \exp\{-(r-0.5)/1.0\}^2$ ,  $T_e/T_i=3$ , and safety factor  $q=0.854+2.184r^2$ . For local FULL simulations, the corresponding parameters used are  $r/R_0=0.175$ ,  $R_0/L_n=R_0/L_{T_e}=6.0$ ,  $R_0/L_{T_i}=1.0$ ,  $q=1.4$ , and magnetic shear  $\hat{s}=(r/q)dq/dr=0.78$ . For the benchmark, the GTS simulation, which is always global, is carried out in a radial domain from 0.1 to 0.9 (in terms of normalized minor radius), and the TEM instabilities are measured at  $r=0.5$ . Note that the magnetic axis is not included in the simulation domain in this study based on considerations from both physical and numerical aspects. First, numerical MHD equilibria expressed in magnetic coordinates, which are currently used by GTS, usually have insufficient resolution near the magnetic axis due to mapping from the original cylindrical coordinates. This may cause numerical problems when simulation particles get into the region. Furthermore, plasma profiles are usually flat in the region near the magnetic axis, which make the region not essential for turbulence physics.

The linear benchmark results are presented in Fig. 1. The growth rates  $\gamma$  and the real frequencies  $\omega_r$  from the global GTS calculation are slightly higher than the local eigenvalue FULL calculation. The overall difference is less than 10%. There are a few effects that may contribute to the difference. First, in particular, FULL is radially local, whereas GTS is radially global. Further, as a subtle detail in this benchmark simulation, GTS includes multiple (all) toroidal modes, which start at very low levels initially ( $e\delta\Phi/T \sim 10^{-15}$ ) so that interactions between the modes are negligible during the linear phase, whereas FULL calculates a single- $n$  mode. Finally, as previously reported, differences in magnetic geometry between the “ $s-\alpha$ ” model and an MHD equilibrium may contribute to discrepancies in gyrokinetic turbulence calculation results.<sup>22</sup> It is also often observed in local linear calculations using the FULL code that the linear frequency and growth rate are rather sensitive to subtle differences of Shafranov shift and finite aspect ratio corrections in the equilibrium. Taking into account all these distinctions between the two simulation models, the overall agreement is reasonable. As a non-

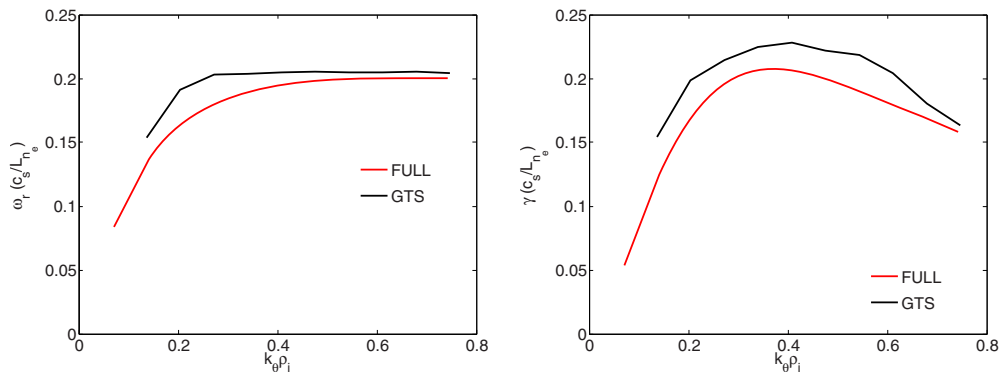


FIG. 1. (Color online) Growth rate  $\gamma$  and real frequency  $\omega_r$  for TEM instability vs poloidal wavenumber  $k_\theta$ , compared with the FULL code calculation.

linear benchmark effort, GTS global and Gyrokinetic ElectroMagnetic (GEM) (Ref. 23) local simulations were carried out for  $\nabla T_e$ -driven CTEM turbulence in a specific, experimentally relevant parameter regime.<sup>24</sup> The purpose of these simulations is to verify the nonlinear generation of bloblike, large fluctuation structures with toroidal mode number  $n \lesssim 10$  via dramatic inverse toroidal energy cascades, and they are beyond the scope of this paper and will be discussed elsewhere in a future publication.

Unlike ITG turbulence with adiabatic electrons, nonadiabatic electron dynamics can drive particle transport for turbulence such as TEM. It is well known that turbulence driven particle transport across the magnetic field lines is ambipolar, i.e., flux-surface-averaged radial particle fluxes for electrons and ions are equal, so as to maintain the overall quasineutrality in a toroidal system. The ambipolarity property of TEM driven cross-field particle transport is tested in the GTS simulation. The time history of particle fluxes (at  $r/a=0.54$ ) is plotted in Fig. 2, showing that electron and ion fluxes very closely track with each other all the time during the simulation. Moreover, the ambipolarity of turbulence driven particle transport is obtained locally over the entire radial domain ( $0.1 \leq r \leq 0.9$ ) of the global simulation, as is seen in the right panel of Fig. 2, which plots the steady state particle fluxes versus minor radius  $r$ . This guarantees that quasineutrality is satisfied radially locally.

Global gyrokinetic turbulence is characterized by distinguishable dynamical phases in both coordinate space and wavenumber space.<sup>25</sup> Ideally, the dynamics of gyrokinetic turbulence should be robust to numerical techniques. The robustness of turbulence dynamics with respect to different approaches for solving the gyrokinetic Poisson equation, the size of the simulation grids and the number of simulation particles, was carefully examined for ITG simulations previously.<sup>7</sup> A further convergence study for CTEM turbulence is presented in Fig. 3. Two simulations using 50 and 100 particles/cell·species, respectively, are shown to produce well converged results for electron particle transport that displays no noticeable difference in a statistical sense (left panel). In other words, the difference in the simulated fluxes between the two cases using 50 and 100 particles/cell·species is within the same range of statistical error of different simulation runs with the same number of particles but with different initial conditions. In the mean time, the time evolution of corresponding average electron weight squared,  $\langle w^2 \rangle$ , of the two simulations is shown to be almost identical (right panel). This result indicates that the observed weight growth does not depend on whether 50 or 100 particles/cell·species are used in these simulations and is driven by physics, corresponding to the increase of amplitude of  $\delta f$  associated with plasma profile evolution induced

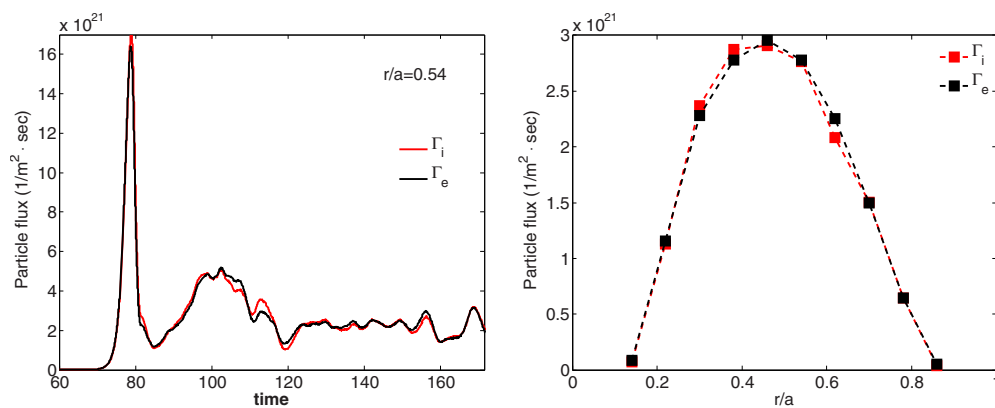


FIG. 2. (Color online) Time history of ion and electron particle fluxes (left) and steady state ion and electron particle fluxes vs minor radius  $r$  (right). Time unit is  $L_n/c_s$ . This is from the same simulation as that in Fig. 1.

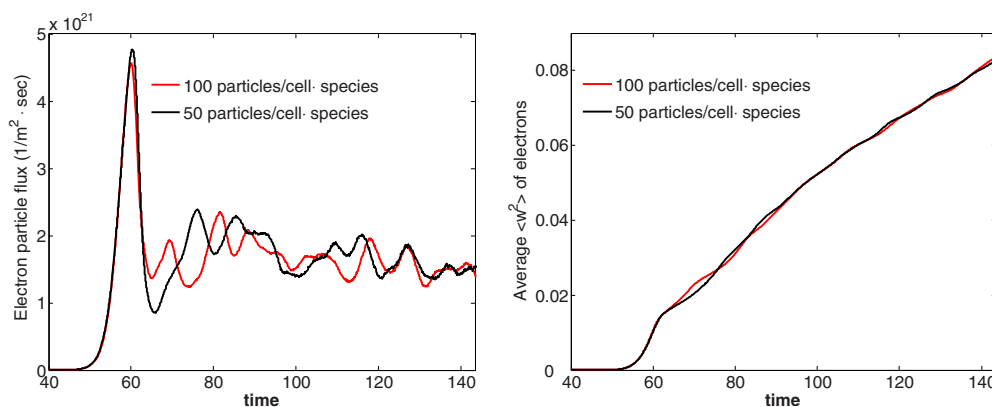


FIG. 3. (Color online) Time history of electron particle fluxes (left) and average weight squares of electrons (right) from two simulations using different number of simulation particle. Time unit is  $L_{T_e}/c_s$ . The major parameters used are  $R_0/L_{T_e}=R_0/L_n=6.5$  and  $R_0/L_{T_i}=2.4$ . A shaped DIII-D type MHD equilibrium is used.

by turbulence driven fluxes during the transport time scale. Furthermore, while the particle weight is physically growing during the simulations, there is no observable correlation between the weight evolution and the dynamics of electron particle flux, as is shown in Fig. 3. The particle weight remains at a low level ( $\langle w^2 \rangle < 0.09$ ) at the end of the simulations, which does not impact the results of simulated transport. These convergence studies clearly indicate that the noise-induced transport in our simulations is negligible with respect to turbulence driven transport. For most simulations in this studies, we use 100 particles/cell-species.

### III. MOMENTUM FLUX PARTITION AND PRANDTL NUMBER

In this section, we first present generic pictures of turbulence driven toroidal momentum transport based on global gyrokinetic simulation results. We then discuss the relationship between the momentum and the energy transport. The critical quantity in the discussion is the Prandtl number, i.e., the ratio of ion momentum and thermal diffusivities,  $\chi_\phi/\chi_i$ , which has attracted a lot of attention in experimental and theoretical studies. It is also highly interesting to examine the partition of the turbulence driven momentum flux, particularly the percentage of the nondiffusive component.

As we mentioned before, a generic structure for turbulence driven toroidal momentum flux can be expressed as follows:

$$\Gamma_\phi \propto -\chi_\phi \frac{\partial U_\phi}{\partial r} + V_p U_\phi + \Pi_{r,\phi}^{\text{rs}}. \quad (10)$$

The three components, diffusion, momentum pinch, and the residual stress, are highly distinctive not only formally but also physically and have different effects on toroidal flow formation. The distinction among the three components, however, is a highly nontrivial task in practice, particularly in experiments. This formulaic difference can be used to design simulations and experiments for the identification and partition of the three components, as in our following numerical studies.

The relationship between turbulence driven toroidal momentum and energy transport has long been an issue of in-

terest in both experimental and theoretical investigations. Experiments on various machines have established a fairly comprehensive database over various regimes, including L-mode and H-mode plasmas, for the ratio of effective momentum and thermal diffusivity,  $\chi_\phi^{\text{eff}}/\chi_i$ , also referred to as the raw Prandtl number. As a general validation against the experimental database, systematic simulations have been carried out over a wide range of experimentally relevant plasma parameters to investigate this issue with a focus on the Prandtl number. The results of this simulation study are summarized below.

At first, it is helpful to write down precisely definitions used to calculate the relevant quantities in the simulations. The effective momentum diffusivity  $\chi_\phi^{\text{eff}}$  and the associated total (net) radial flux of toroidal momentum  $\Gamma_\phi$  are calculated according to the following expression, which is suitable for general geometry:

$$\begin{aligned} \Gamma_\phi &\equiv \left\langle \int d^3v m_i R v_\phi \mathbf{v}_E \cdot \nabla \rho / |\nabla \rho| \delta f_i \right\rangle \\ &\equiv -m_i n_i \chi_\phi^{\text{eff}}(\rho) \langle R^2 |\nabla \rho| \rangle \frac{d\omega_\phi}{d\rho}, \end{aligned} \quad (11)$$

where  $\rho$  is a radial coordinate denoting magnetic flux surface.

In ion-dynamics-dominated regimes, our simulations verify that there exists strong coupling between ion momentum and heat transport for ITG driven turbulence, and the effective  $\chi_\phi^{\text{eff}}/\chi_i$  is on the order of unity. This is in broad agreement with a theoretically predicted trend<sup>5</sup> and experimental observations<sup>6</sup> in conventional tokamaks where low- $k$  fluctuations are believed to be responsible for a high level of plasma transport. A typical simulation result is shown in Fig. 4, where  $\chi_\phi^{\text{eff}}/\chi_i \sim 1$  is obtained in the long-time steady state. On the other hand, global gyrokinetic turbulence is characterized by distinguishable dynamical phases in both configuration space and wavenumber space, and correspondingly the turbulence driven momentum transport can display different behavior over different dynamical phases of turbulence evolution and the Prandtl number varies. Particularly in the ITG turbulence regime with adiabatic electrons, a significant in-

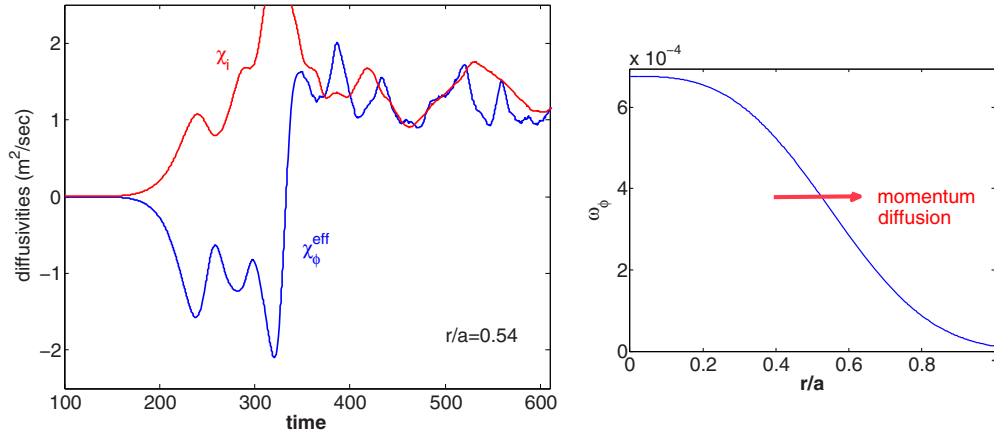


FIG. 4. (Color online) Time evolution of effective toroidal momentum and heat diffusivity (left) and initial toroidal rotation profile (right). Time unit is  $L_{T_i}/v_{\text{th}}$ .

ward, nondiffusive momentum flux associated with residual stress is robustly observed in the post saturation phase,<sup>26</sup> which is after the nonlinear saturation of the ITG instability but before a long term steady state. As is seen in Fig. 4, there is an up-gradient momentum flux generated in the postsaturation phase. This nondiffusive flux can result in a great departure of the Prandtl number from unity. Moreover, the Prandtl number in the long-time steady state is also shown to vary over a certain range around unity, showing fairly sensitive dependence on plasma parameters. Finally, as a further validation effort, GTS simulation predictions of toroidal momentum and ion thermal transport have been directly compared with experimental measurements on DIII-D. Results for an ion transport dominated DIII-D discharge with relatively high toroidal rotation are presented in Fig. 5. Reasonably good agreement between the simulation of ITG turbulence and the experiment is obtained not only for the Prandtl number but also for the individual values of  $\chi_\phi$  and  $\chi_i$ .

The calculation of the raw Prandtl number in experiments is relatively straightforward (many experimental results reported are raw Prandtl number). While it is useful to look at the raw Prandtl number, a more meaningful physics quantity to examine is the ratio of pure momentum diffusivity and thermal diffusivity,  $\chi_\phi/\chi_i$ , which is referred as the intrinsic Prandtl number  $P_r$ , though it is harder to calculate. Obviously,  $P_r = P_r^{\text{raw}}$  if there is no nondiffusive contribution to the momentum flux, and the difference between the two reflects the fraction of nondiffusive contributions. Specifically, the ratio of nondiffusive and total momentum flux  $\Gamma_\phi^{\text{nd}}/\Gamma_\phi = 1 - P_r/P_r^{\text{raw}}$ .

An intrinsic Prandtl number of unity was theoretically predicted for drift wave turbulence.<sup>5</sup> Recent studies indicate departures of  $P_r$  from unity.<sup>12,27</sup> To obtain the intrinsic  $P_r$ , one has to separate out the nondiffusive components from the total momentum flux, which is a highly nontrivial task, particularly in experimental measurements. To this end, a set of numerical experiments has been carefully designed and carried out. In these simulations, toroidal rotation profiles are set to have zero rotation velocity at normalized minor radius  $\rho_c = 0.5$  and to have a step-type profile of the following form for the rotation gradient:

$$\frac{d\omega_\phi}{d\rho} = \kappa_{\omega_\phi} \exp\left[-\left(\frac{\rho - \rho_c}{\Delta\rho}\right)^\alpha\right],$$

with  $\alpha=6$  and  $\Delta\rho=0.28$ . Here we use ITG turbulence with adiabatic electrons. We are first look at the marginally unstable ITG regime using two simulations with  $R_0/L_{T_i}=5.5$  and  $T_e/T_i=1$ . For both simulations, only one parameter  $\kappa_{\omega_\phi}$  varies, which corresponds to the use of different initial rotation gradients. The simulation domain is from  $\rho=0.1$  to  $0.9$ , and we focus on a narrow radial annulus centered at  $\rho_c$ , where the rotation velocity and the momentum pinch vanish. The remaining nondiffusive component of momentum flux in the region is the residual stress, which is independent of the variation of the rotation gradient. From Eqs. (10) and (11), we have

$$P_r^{\text{raw}} = P_r - \frac{\Pi_{r,\phi}^{\text{rs}}}{c_g \chi_i} \frac{1}{d\omega_\phi/d\rho},$$

where  $c_g = m_i n_i \langle R^2 |\nabla\rho| \rangle$  is a geometry factor. The key idea for these simulations to allow for separation of the diffusive and

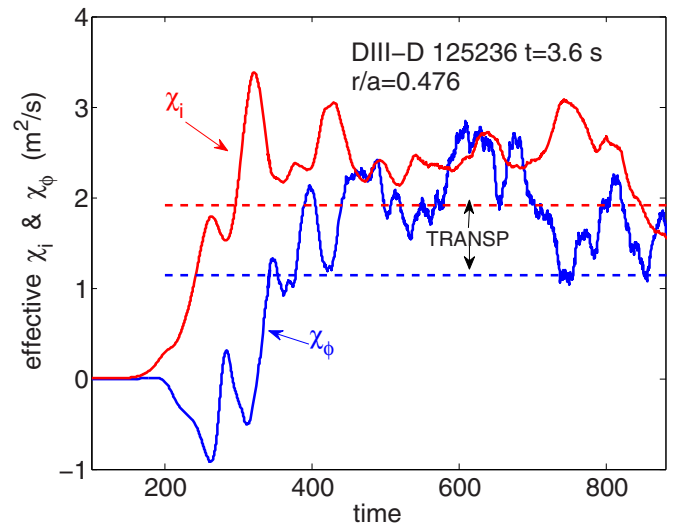


FIG. 5. (Color online) Time history of ITG turbulence driven effective  $\chi_\phi^{\text{eff}}$  and  $\chi_i$  from a simulation of a DIII-D discharge and comparison with experimental results from TRANSP analysis. Time unit is  $L_{T_i}/v_{\text{th}}$ .

nondiffusive components is based on the fact that the shear flow instability is very hard to drive unstable in a toroidal system because of the strong stabilization effect of the magnetic shear. However, the equilibrium (mean)  $\mathbf{E} \times \mathbf{B}$  shear flow, which is determined by neoclassical dynamics to relate to the toroidal rotation via the radial force balance relation, can influence both turbulence and residual stress generation. For simplicity, we exclude the equilibrium electric field in these simulations. In this case, we expect that rotation, particularly with relatively low gradient, has negligible effect on ITG driven turbulence, i.e., fairly similar turbulence fields can be produced in the two cases with different rotations. Hence, it is reasonable to argue that  $P_r$  and  $\Pi_{r,\phi}^{rs}/\chi_i$  are held constant in these simulations. (Note that turbulence intensity may slightly vary from one simulation to another. While both  $\chi_\phi$  and  $\chi_i$  are each roughly proportional to the intensity, the ratio  $P_r$  is less sensitive to the intensity variation. So is the quantity  $\Pi_{r,\phi}^{rs}/\chi_i$ .) Therefore, from two aforementioned simulations I and II, we can estimate the intrinsic Prandtl number using

$$P_r = \frac{P_r^{\text{raw,I}}(d\omega_\phi^{\text{I}}/d\rho) - P_r^{\text{raw,II}}(d\omega_\phi^{\text{II}}/d\rho)}{d\omega_\phi^{\text{I}}/d\rho - d\omega_\phi^{\text{II}}/d\rho}. \quad (12)$$

Figure 6 (top panel) shows the time history of  $P_r^{\text{raw}}$ , from linear phase to saturated steady state, of two simulations with  $d\omega_\phi^{\text{II}}/d\rho = 2 \times d\omega_\phi^{\text{I}}/d\rho$ . Note that a semiquantitative definition should be used for “steady state,” relative to linear growth and postsaturation phases, particularly in a global simulation. Specifically, the time averaged growth rate of the turbulence intensity vanishes, relative to the linear growth rate, though the instantaneous growth rate fluctuates. On the other hand, the toroidal spectra of fluctuations in the steady state turbulence regime, which can be used for comparison with experimental measurements in validation studies, are typically characterized by a significant downshift from linearly unstable modes due to nonlinear toroidal energy cascades.<sup>25</sup> However, a steady state may still exhibit considerable temporal variations in various transport quantities, particularly in a global simulation, due to mesoscale dynamics such as turbulence spreading, self-consistent plasma profile evolution, turbulence avalanches, etc. As is generally done for calculating transport fluxes in this type of turbulence simulation studies, an averaged raw Prandtl number in the saturated turbulence steady state is calculated by time average. Generally, the interval of time averaging should be some time scale between the correlation time and the profile evolution time. In this case, an averaged raw Prandtl number is calculated over a period from  $t=1000$  to  $2400$ , which spans many turbulence growth times. The obtained values are  $P_r^{\text{raw,I}} = 0.961 \pm \sigma$  and  $P_r^{\text{raw,II}} = 0.703 \pm \sigma$  in the two cases with the standard deviations  $\sigma = 0.19$  and  $0.14$ , respectively. These results, in terms of Eq. (12), give an estimate  $P_r = 0.445$  for the intrinsic Prandtl number in the marginal ITG regime. This result appears to be consistent with a recent theoretical prediction of  $P_r \sim 0.2-0.5$  in stiff profile regimes.<sup>12</sup>

Plotted in the middle of Fig. 6 is a scan of  $P_r$  versus  $R_0/L_{Ti}$ , showing that the intrinsic Prandtl number increases with the temperature gradient. The ratio between the residual

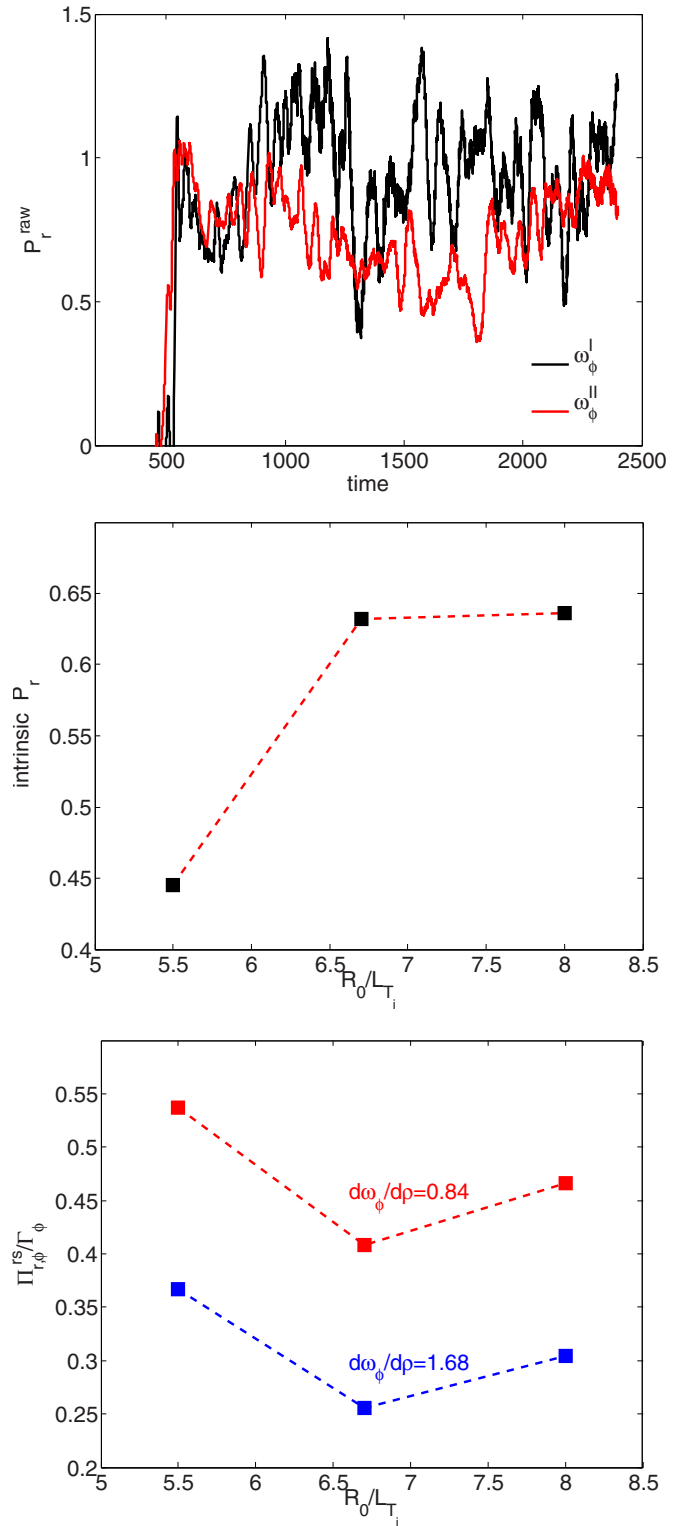


FIG. 6. (Color online) Time (normalized by  $L_T/v_{th}$ ) evolution of raw Prandtl number from two simulation with  $R_0/L_{Ti} = 5.5$  and different rotation gradients (top), intrinsic Prandtl number vs  $R_0/L_{Ti}$  (middle), and ratio of residual stress over total momentum flux vs rotation gradient and  $R_0/L_{Ti}$  (bottom).

stress component and the total momentum flux is plotted at the bottom of Fig. 6, which shows that the residual stress contribution to the total momentum flux is significant (more than 50% for case I), and is increased with the decrease of



the rotation gradient. This is readily understandable because the residual stress, unlike the diffusive component, is independent of rotation gradient. On the other hand, the fraction of residual stress does not show a clear, conclusive scaling trend with  $R_0/L_{T_i}$ .

#### IV. NONLINEAR RESIDUAL STRESS GENERATION AND THE SCALING OF INTRINSIC TORQUE

We have shown that the residual stress component can be a substantial portion of the total momentum flux driven by ITG turbulence. As discussed in the previous section, residual stress, acting as an internal torque, may play a critical role in driving intrinsic rotation. The micropicture of this mechanism is that the net parallel (toroidal) flow is accelerated by turbulence, which critically depends on the details of the parallel wavenumber spectrum. For most drift wave instabilities, both signs of  $k_{\parallel}$  are equally excited, resulting in a reflection symmetry in the  $k_{\parallel}$  spectrum. Perfect local  $k_{\parallel}$  symmetry means perfectly balanced population density between co- and counterpropagating acoustic waves and thus a vanishing net local momentum torque. Therefore, a critical, generic piece of physics behind the residual stress spinning up the plasma is the breaking of the  $k_{\parallel} \rightarrow -k_{\parallel}$  symmetry.

Out of various theoretical possibilities, one of the leading candidates is a mean  $\mathbf{E} \times \mathbf{B}$  flow shear, which shifts the eigenmode to one side radially and thus produces a nonvanishing spectrum-averaged  $k_{\parallel}$ .<sup>10,11,28–30</sup> Another symmetry breaking mechanism, which leads to an inward pinch, can come from the interplay of magnetic field curvature and ballooning mode structure in toroidal geometry.<sup>31,32</sup> See Table I in Ref. 31 for a unified illustration of these two symmetry breaking mechanisms from a gyrokinetic theory viewpoint.

Recently, using global gyrokinetic simulation, a universal mechanism for  $k_{\parallel}$  symmetry breaking has been identified due to turbulence self-generated zonal flow shear,<sup>26</sup> and an associated residual stress has been robustly observed in ITG simulations over a wide range of experimentally relevant parameters. From the viewpoint of local analysis and simulation, the turbulence self-generated zonal flow shear has no preferred direction in a long-time statistical sense and therefore was expected to have little direct effect on the  $k_{\parallel}$  spectrum. However, for global simulations, the zonal flow dynamics is found to be significantly different from the local picture. Specifically, zonal flow is shown to be slowly varying in time and of large scale in space.<sup>17</sup> This is also an indication of the existence of toroidal zonal flow. A slowly varying large scale zonal flow structure has been clearly identified recently in drift wave turbulence in a linear machine.<sup>33</sup> The observed low frequency, large scale zonal flow structure is shown to have a remarkable effect on the parallel spectrum of potential and density fluctuations.

The most straightforward way to examine turbulence driven residual stress is to set the initial rotation to be zero in simulations. Thus, only the residual stress component remains in the momentum flux. To elucidate the critical role of zonal flows in the nonlinear flow generation, unless explicitly specified, equilibrium  $\mathbf{E} \times \mathbf{B}$  flows are excluded in the following simulations. This may correspond to typical core

turbulence apart from internal transport barriers and in L-mode plasmas, where equilibrium shear is not dominant. The quantity used to characterize the  $k_{\parallel}$  symmetry breaking in our study is the average parallel wavenumber of the turbulence spectrum defined as

$$\langle k_{\parallel} \rangle(r) \equiv \frac{1}{qR_0} \frac{\sum (n/|n|)(nq-m)\delta\Phi_{mn}^2}{\sum \delta\Phi_{mn}^2}, \quad (13)$$

where  $\delta\Phi_{mn}$  is a mode amplitude, with  $m$  and  $n$  the poloidal and toroidal mode numbers, respectively,  $q$  is the safety factor, and  $R_0$  is the major radius. Figure 7 illustrates the simulation results of ITG turbulence with adiabatic electrons. For this case, the ITG instability is quite marginal with  $R_0/L_{T_i}=4.9$  and  $T_i=T_e$ . First, the upper-left panel of Fig. 7 shows that a significant inward flux of toroidal momentum is driven in the whole radial range with ITG turbulence present. Particularly, a large inward momentum flux emerges in the postsaturation phase, which is after the nonlinear saturation of the ITG instability but before a long term steady state ( $t \sim 1000-1800$ ). Because of the zero initial toroidal rotation used, the momentum flux is, by definition, essentially residual stress. Plotted in the lower-left panel is  $\sum k_{\parallel} \delta\Phi_{mn}^2$  which is a quantity resembling the residual stress expression. One can see that  $\sum k_{\parallel} \delta\Phi_{mn}^2$  indeed reproduces a similar spatiotemporal behavior to the directly calculated momentum flux. Further, in the upper-right panel, the spectrum-averaged  $k_{\parallel}$  shows an apparent spatiotemporal correlation with  $\Gamma_{\phi}$ , indicating the importance of nonvanishing  $\langle k_{\parallel} \rangle$ . The whole picture for the residual stress generation is completed by finding out what causes  $k_{\parallel}$  symmetry breaking, giving rise to the nonzero  $\langle k_{\parallel} \rangle$ . This is in the lower-right panel, which plots the shearing rate of turbulence self-generated zonal flows according to a formula for shaped tokamak geometry,<sup>34</sup>

$$\omega_E^{ZF} = \frac{R^2 B_p^2}{B} \frac{\partial}{\partial \Psi_p} \left( \frac{E^{ZF}}{RB_p} \right), \quad (14)$$

where  $B$  and  $B_p$  are the total and poloidal magnetic field strengths and  $\Psi_p$  is the poloidal magnetic flux. A clear correlation between the zonal flow shearing rate  $\omega_E^{ZF}$  and  $\langle k_{\parallel} \rangle$  indicates that the breaking of  $k_{\parallel}$  symmetry and the yielding of nonvanishing  $\langle k_{\parallel} \rangle$  are caused by the zonal flow shear. Since zonal flows are turbulence self-generated, this process represents a universal, nonlinear mechanism for residual generation. It is expected to play an important role in flow generation, particularly in L-mode plasmas where the  $\mathbf{E} \times \mathbf{B}$  shear of the equilibrium electric field is weak.

As discussed previously, residual stress, acting like an intrinsic (internal) torque, is the only way to spin up a plasma from rest. The observation that an external torque in the countercurrent direction is required to hold the plasma from rotating is another direct evidence of the existence of intrinsic torque.<sup>35</sup> Recently, intensive experimental studies carried out on various machines attempted to identify the role of residual stress and to characterize the dependence of the intrinsic rotation and intrinsic torque on plasma parameters. The empirical tendency obtained in H-mode plasmas shows that the offset value of the toroidal rotation typically scales with the increment in stored energy, and the rotation is

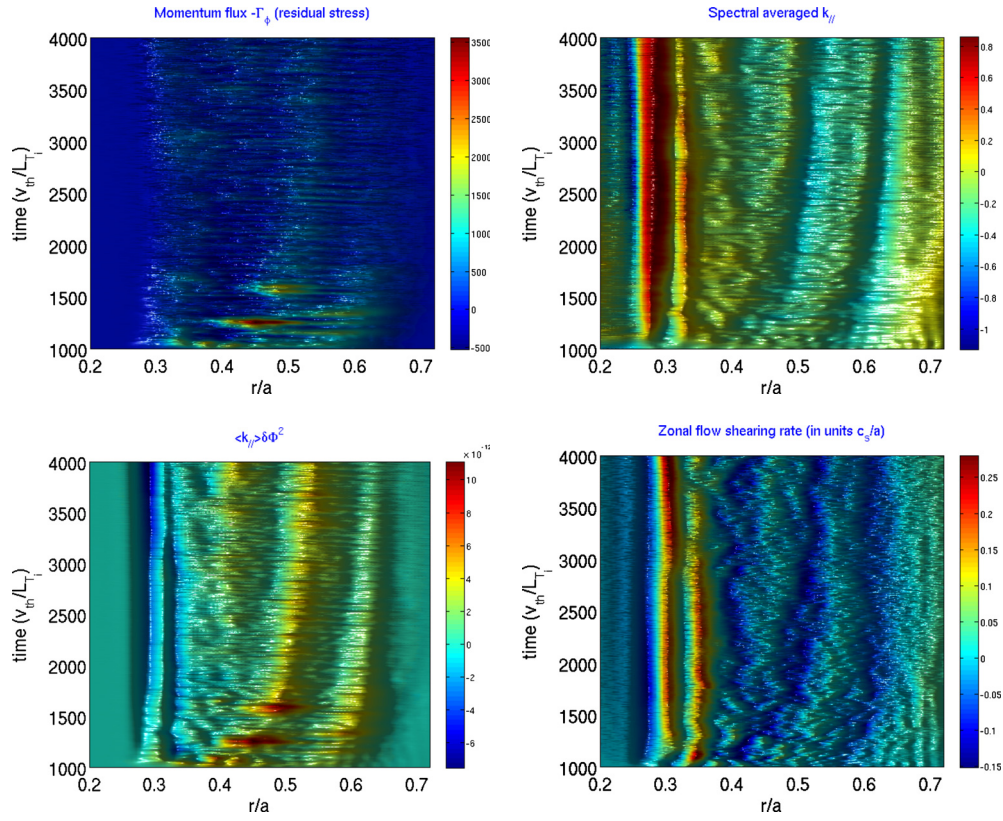


FIG. 7. (Color online) Spatiotemporal evolution of radial flux of toroidal momentum (upper-left),  $\langle k_{\parallel} \rangle \Sigma \delta \Phi_{min}^2$  (lower-left), spectrum-averaged  $\langle k_{\parallel} \rangle$  (upper-right), and zonal flow shearing rate (lower-right).

usually in the cocurrent direction.<sup>36</sup> Intrinsic rotations are observed to increase with increasing pressure gradient in various JT-60 plasmas.<sup>37</sup>

The characteristic dependence of intrinsic torque driven by ITG turbulence is investigated using a set of systematic simulations. The radial profiles of ion temperature are given by specifying a temperature gradient profile according to the following form:

$$R_0/L_{T_i} = -\kappa_{T_i} \exp\left[-\left(\frac{\rho - \rho_c}{\Delta\rho}\right)^\alpha\right],$$

along with a fixed temperature  $T_i = 1$  KeV at  $\rho_c = 0.5$ . This gives a fairly uniform ITG drive in a region centered at  $\rho_c$ , as shown in the top panel of Fig. 8. The temperature gradient varies from  $\kappa_{T_i} = 4.9$  to 8.2 for these simulations, covering a wide range from near to well beyond ITG marginality. The rest of the input parameters are the same for all six simulations.

The intrinsic momentum torque appearing in the toroidal momentum balance (transport) equation takes the form  $\nabla \cdot \mathbf{\Pi}_{r,\phi}^{RS}$ . Instead of calculating the local torque  $\nabla \cdot \mathbf{\Pi}_{r,\phi}^{RS}$ , we examine the rate of toroidal momentum generation due to ITG turbulence. The residual stress is the only source responsible for the momentum build-up in this case. The midpanel of Fig. 8 illustrates the spatiotemporal evolution of flux-surfaced averaged toroidal momentum density  $\langle p_\phi \rangle$  with  $p_\phi$  defined as  $p_\phi \equiv \int d^3v m_i R v_\phi \delta f_i$ . The quantity calculated here is the rate of total toroidal momentum generation  $dP_\phi/dt$ , where  $P_\phi \equiv \int d^3r |p_\phi|$ . Apparently, the quantity  $dP_\phi/dt$  is a

measure of total (or spatially averaged) torque driven by turbulence, which has better correspondence to the intrinsic torque inferred from experiments. As illustrated in Fig. 8 (bottom), the ITG driven intrinsic torque is shown to increase with the temperature gradient. A slightly stronger than linear scan of torque versus  $R_0/L_{T_i}$  (and equivalently, torque versus  $R_0/L_p$  because of the fixed density profile used in all these simulations) is obtained. This result is consistent with experimental trends observed in various devices,<sup>37–39</sup> including Alcator C-MOD where the central flow velocity scales linearly with the edge pressure gradient.

The dominant underlying physics governing this characteristic dependence is that the residual stress is proportional to the turbulence intensity, which, in turn, is increased with the strength of the ITG drive  $R_0/L_{T_i}$ . However, this does not explicitly give a linear dependence from a simple argument. The zonal flows and their effect on  $k_{\parallel}$  symmetry breaking, on the other hand, are also expected to increase with the increase of turbulence intensity. Therefore, we may expect a stronger than linear scan of torque versus  $R_0/L_{T_i}$  for the nonlinearly driven residual stress. It is noticed that the dependence on pressure gradient can also be introduced via the equilibrium radial electric field (not included in these simulations), which relates to the pressure gradient through the well known radial force balance relation. However, this connection is less transparent. First of all, the equilibrium  $\mathbf{E} \times \mathbf{B}$  flow shear effects are twofold: reducing fluctuation intensity and breaking up  $k_{\parallel}$  symmetry. Its overall effect on residual stress generation depends on the balance between

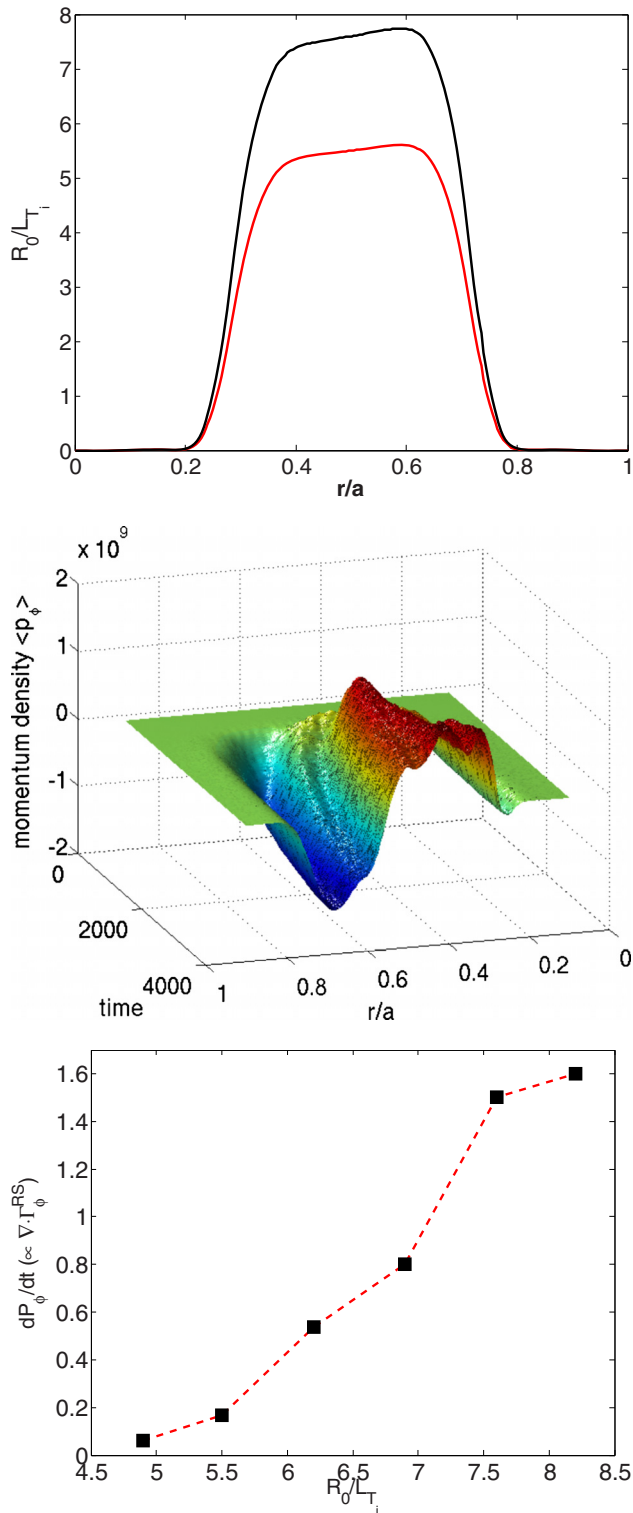


FIG. 8. (Color online) Radial profiles of  $R_0/L_{T_i}$  (illustrated are two cases with  $\kappa_{T_i}=5.5$  and  $7.6$ ; top); spatiotemporal evolution of toroidal momentum density  $\langle p_\phi \rangle$  (flux-surface averaged; middle); and total intrinsic torque (spatially averaged) vs ion temperature gradient  $R_0/L_{T_i}$  (bottom).

the two. Second, the mean  $\mathbf{E} \times \mathbf{B}$  shear is proportional to both  $d^2p/dr^2$  and  $(dn/dr)(dp/dr)$ . It should be pointed out that the scaling of the torque versus  $\nabla p$  does not hold locally. For instance, one can have zero local torque, i.e., the divergence of the residual stress is zero, at a location of strong  $\nabla T$  and maximal residual stress.

The nonlinear residual stress generation is also observed for electron driven turbulence such as CTEM. We will present these results in the next section. The characteristic dependence of associated residual stress driven torque on gradients of electron profiles, such as  $\nabla T_e$ ,  $\nabla n_e$ , and  $\nabla p_e$ , can be established through electron driven turbulence. Even more complex connections are expected between the intrinsic torque and plasma profiles in the presence of hybrid ITG/TEM turbulence, which is more likely to be the case in experiments. However, all these are beyond the scope of this paper and will be discussed elsewhere in future publications.

## V. NONLINEAR RESIDUAL STRESS GENERATION IN CTEM TURBULENCE AND TRAPPED ELECTRON EFFECTS IN ITG REGIME

In this section, we discuss the effects of trapped electrons, focusing on nonlinear residual stress generation by TEM turbulence and ITG turbulence with nonadiabatic electrons. For simulations with kinetic electrons presented in this section and hereafter, unless explicitly specified, the working gas is hydrogen, i.e., the ion-electron mass ratio is  $m_i/m_e=1836$ .

We first examine ITG turbulence. The major parameters used are  $R_0/L_{T_i}=5.3$ ,  $R_0/L_{T_e}=1.6$ ,  $R_0/L_n \lesssim 1$ , and initial rotation  $\omega_\phi=0$ . For these parameters, the ITG modes are marginally unstable, as found in many experiments,<sup>6</sup> and TEM modes are stable. This allows us to investigate the same turbulence (i.e., ITG) when we switch the electron response in the simulations from adiabatic to nonadiabatic. Figure 9 shows the results of ITG turbulence with adiabatic electrons. Similar to Fig. 7, close spatiotemporal correlations among the momentum flux  $\Gamma_\phi$ ,  $\Sigma k_\parallel \delta \Phi_{mn}^2$ , the spectrum average  $\langle k_\parallel \rangle$ , and the zonal flow shearing rate  $\omega_E^{\text{ZF}}$  illustrated in Fig. 9 clearly demonstrate that the residual stress is nonlinearly driven by the fluctuation intensity, acting with the zonal flow shear, which induces symmetry breaking in the  $k_\parallel$  spectrum.

The results for ITG turbulence with nonadiabatic electrons are presented in Fig. 10, which uses exactly the same set of simulation parameters as in Fig. 9. An immediate observation is that the spatiotemporal correlations among the plotted four quantities become obviously less clear, compared to the ITG case with adiabatic electrons (Fig. 9). First, the lesser similarity in spatiotemporal structures between the momentum flux (residual stress, upper-left panel) directly calculated from Eq. (11) and an estimate of  $\Sigma k_\parallel \delta \Phi_{mn}^2$  (lower-left) indicates that the turbulence intensity driven residual stress does not fully account for the residual stress produced by the turbulence. Further, less correlation in spatiotemporal structures between  $\langle k_\parallel \rangle$  (upper-right) and  $\omega_E^{\text{ZF}}$  (lower-right) indicates that the zonal flow shear does not fully account for the origin of nonvanishing  $\langle k_\parallel \rangle$ . The nonadiabatic electrons are shown to introduce finer radial scales into the zonal flows. In the configuration space, this appears as small wiggles (finer structures with small amplitude) sitting on a large scale structure with large amplitude. The corresponding  $\mathbf{E} \times \mathbf{B}$  shear at small scales and low frequencies, however, appears too weak to have a visible impact on the  $k_\parallel$  spectrum (upper-right and lower-right panels). The key points made by

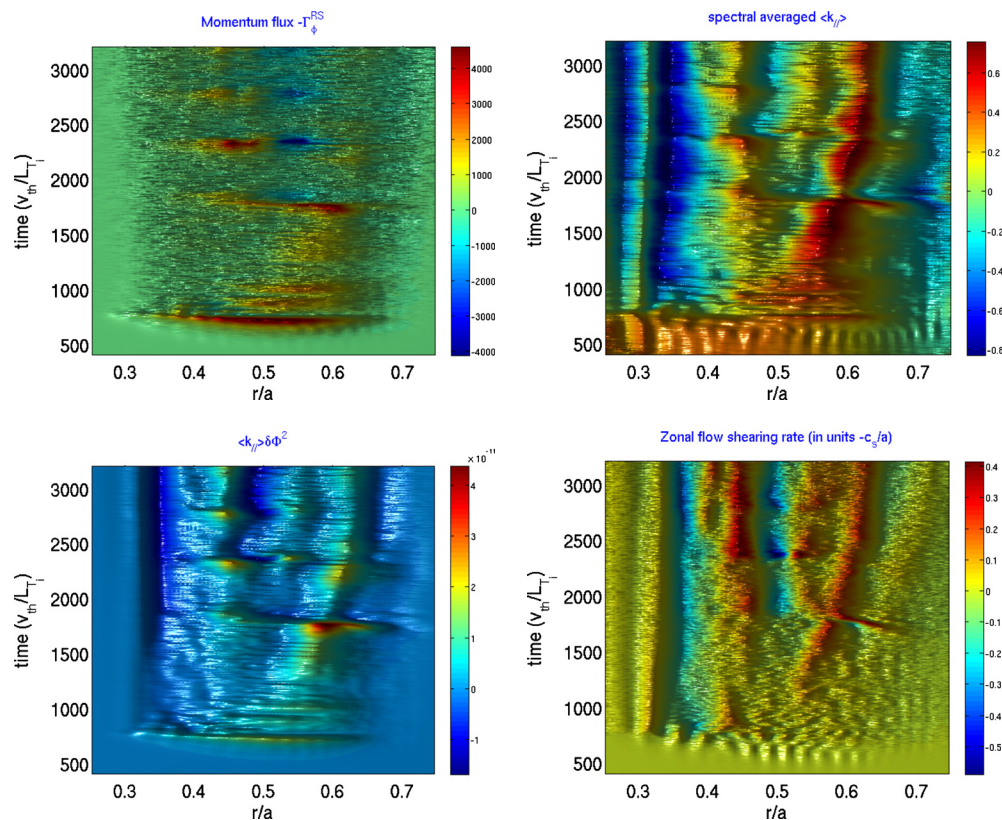


FIG. 9. (Color online) Spatiotemporal evolution of radial flux of toroidal momentum (upper-left),  $\langle k_{\parallel} \rangle \Sigma \delta \Phi_{mn}^2$  (lower-left), spectrum-averaged  $\langle k_{\parallel} \rangle$  (upper-right), and zonal flow shearing rate (lower-right) from ITG simulation with adiabatic electrons.

these results clearly indicate (i) the existence of other possibilities for driving residual stress and (ii) the existence of other mechanisms beyond  $\mathbf{E} \times \mathbf{B}$  shear for  $k_{\parallel}$  symmetry breaking. For the former, one interesting candidate is the turbulence intensity gradient<sup>12</sup> whose important role will be elucidated in our CTEM simulations to be presented later. For the latter, the possible mechanisms include the effects of magnetic shear, nonlinear mode couplings, and turbulent radial current, which will be addressed in a future publication.

Now we present a simulation of an experimental case, which shows trapped electron effects on ion turbulence and transport. Simulation results presented in Fig. 11 are for a DIII-D experiment. This is an ion transport dominated DIII-D discharge with low toroidal rotation. A relatively large ion temperature gradient exists in the range of  $r/a \sim 0.2-0.5$ , which makes ITG modes unstable, while TEMs are stable for most minor radii. The real mass ratio  $m_i/m_e = 3672$  for deuterium plasma is used in this simulation. As is illustrated in the left panel of Fig. 11, the ITG turbulence with adiabatic electrons is shown to produce ion heat transport at a much higher level than the neoclassical in the inner core area, which matches the experimental level in the region. However, the ITG simulation with adiabatic electrons fails to account for the observed high level ion transport in the outer core region beyond  $r/a \sim 0.45$ , where the ITG instability is marginal or even stable. Trapped electron physics is found to play a critical role in this region. When trapped electrons are included, they substantially destabilize the ITG mode due to the resonance between the mode frequency and

the toroidal precession frequency with a corresponding change in the electron response as compared to the adiabatic case. This resonance occurs for precession drift-reversed trapped electrons and has dependence on the magnetic shear. The net effect of trapped electrons is to increase linear growth rate and nonlinear saturation level. Consequently, ITG driven fluctuation intensity is substantially enhanced, particularly in the outer core region where the pure ITG modes are marginal or stable. As a result, the simulated ion heat flux is increased to be closer to the experimental observations in the region, while the ion transport is not considerably affected in the inner core region where the ITGs are strongly unstable. In the two cases, the core ITG turbulence cannot reproduce the experimental level of ion heat transport in the further outer core region beyond  $r/a > 0.6$ , where ion transport may be largely controlled by edge-core coupling. On the other hand, the ITG driven toroidal momentum flux is also substantially increased by nonadiabatic electrons (the right panel of Fig. 11). For this DIII-D shot, the toroidal rotation is small and flat with  $\omega_{\phi} \sim 10^4$  (1/s) in the region of  $r/a > 0.4$  due to using counter-neutral-beam injection, which balances the intrinsic torque. This implies that the momentum flux observed in the simulation mostly comes from the residual stress.

Now we turn to discussing one of the key results of our simulation study, i.e., nonlinear residual stress and flow generation in CTEM turbulence. The CTEM simulation presented below employs typical parameters of DIII-D plasmas. The major parameters used here are  $R_0/L_{Te} = R_0/L_n = 6.0$ ,

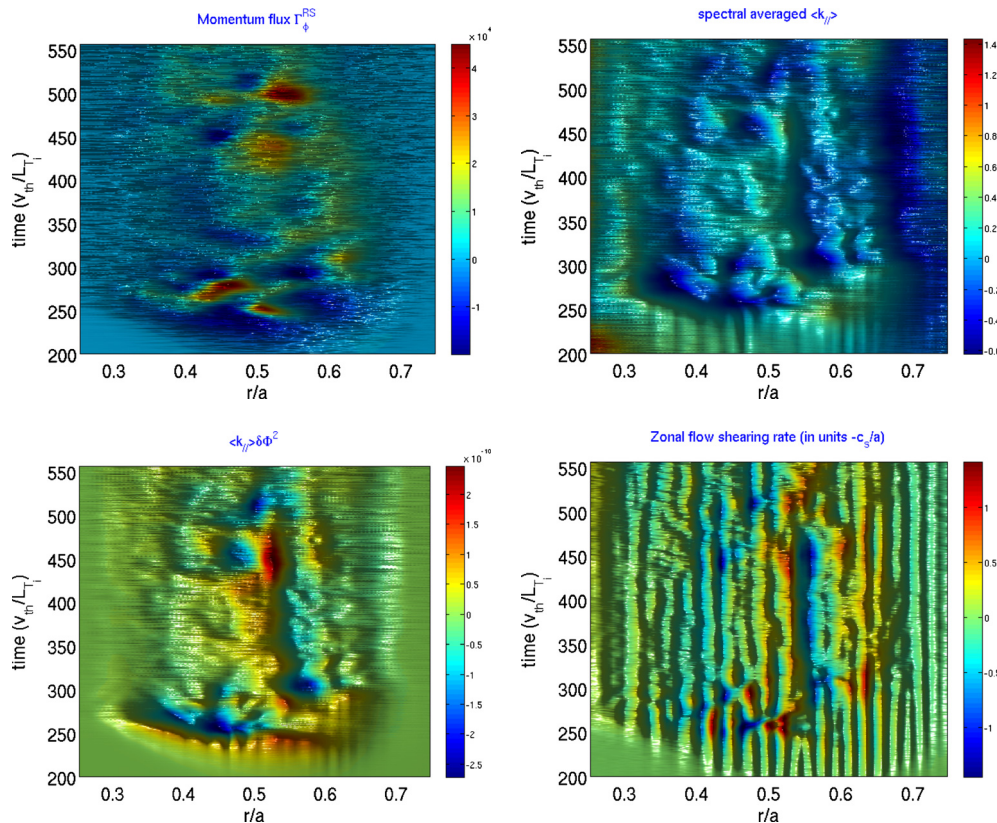


FIG. 10. (Color online) Spatiotemporal evolution of radial flux of toroidal momentum (upper-left),  $\langle k_{\parallel} \rangle \Sigma \delta \Phi_{mn}^2$  (lower-right), spectrum-averaged  $\langle k_{\parallel} \rangle$  (upper-right), and zonal flow shearing rate (lower-right) from ITG simulation with nonadiabatic electrons, which uses the same parameters as in Fig. 9.

$R_0/L_{Ti}=2.4$ ,  $T_e=4.8$  KeV, and  $T_i=3.5$  KeV at  $r/a=0.5$ , and an initial rotation  $\omega_{\phi}=0$ . A numerical MHD equilibrium corresponding to a real DIII-D discharge is used. An equilibrium electric field, which satisfies the radial force balance relation, is also included in this CTEM simulation. As a key player in drift wave turbulence in general and in residual stress gen-

eration specifically, zonal flows generated by global CTEM turbulence display distinct characteristics compared to large scale, stationary ones typically observed in global ITG turbulence (see the top panel of Fig. 3 in Ref. 26). As illustrated in Fig. 12, in addition to radially global structures with  $k_{\parallel} \rho_s \sim 0$ , which are dominant, there are significant shorter

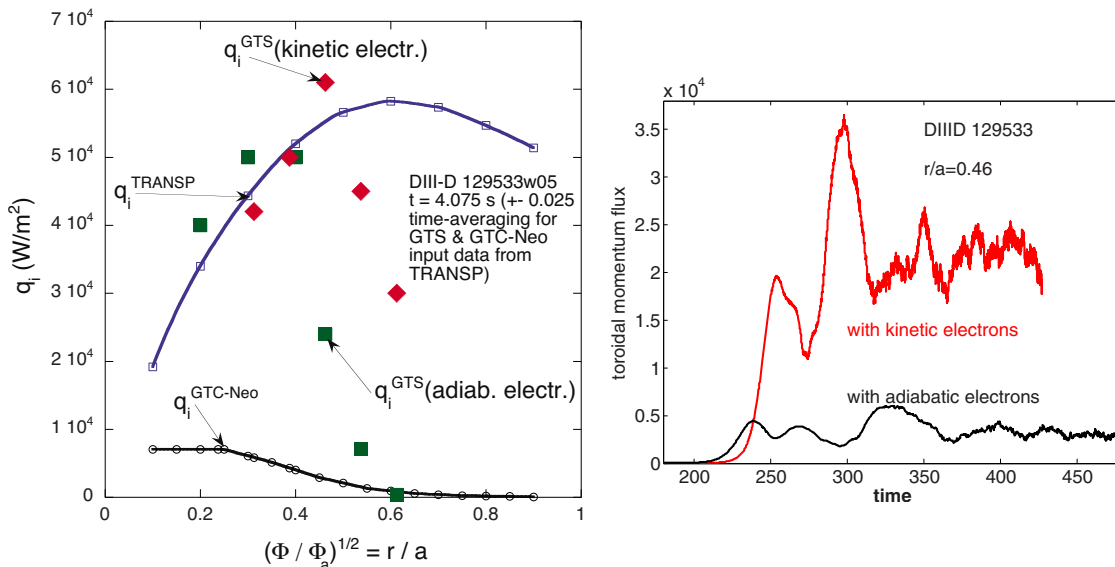


FIG. 11. (Color online) Ion heat fluxes vs  $r/a$  from ITG simulations with adiabatic and nonadiabatic electrons and comparison with experimental result from TRANSP and neoclassical level from GTC-NEO (Ref. 19) (left) and time history of ITG driven toroidal momentum fluxes (right), showing enhancement due to trapped electrons.

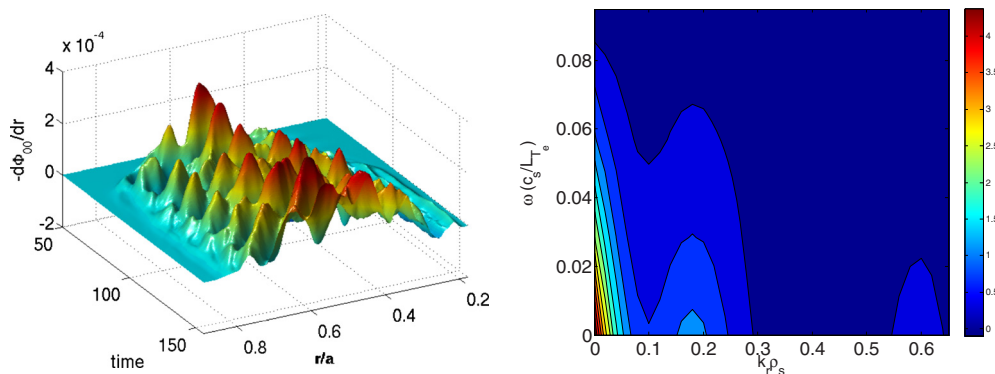


FIG. 12. (Color online) Spatiotemporal evolution of zonal flows generated in CTEM turbulence (left) and corresponding spectra in  $(\omega, k_r)$  space (right).

scale structures with  $k_r \rho_s \sim 0.2$  and even fine (but weak) structures at  $k_r \rho_s \sim 0.6$ . Recent theoretical calculations of zonal flow growth rate indicate the zonal flow generation at fine-scales with  $k_r \rho_i \sim 1$  in CTEM turbulence.<sup>40</sup> The zonal flows are also shown to be less stationary, exhibiting significant temporal variation in amplitude. In the frequency domain, the zonal flows peak at zero frequency but with a certain extension to the low frequency range. At the same time, the zonal flow component at the geodesic acoustic frequency is very weak. The zonal flow shearing rate, however, is high, which is shown to have a strong effect on the turbulence parallel wavenumber spectrum.

The nonlinear residual stress generation by CTEM turbulence, for the first time, is clearly observed in global simulations, as illustrated in Fig. 13. First, the CTEM-driven residual stress exhibits coherent spatiotemporal bursting behavior with momentum flux pulses propagating both inward and outward in the radial direction, as shown in the top-left panel of Fig. 13. The residual stress at steady state changes direction from outward in the inner core region to inward in the outer core region. The midleft panel of Fig. 13 is  $\Sigma k_{\parallel} \delta \Phi_{nm}^2$ , which represents the component of the residual stress driven by the turbulence intensity in the presence of nonvanishing  $\langle k_{\parallel} \rangle$ . The observation of a clear correlation between  $\Gamma_{\phi}^{RS}$  and  $\Sigma k_{\parallel} \delta \Phi_{nm}^2$  indicates that the turbulence intensity plays a major role in driving the residual stress, particularly in the inner core region ( $r/a < 0.55$ ). In the outer core region, however, the turbulence intensity effect appears not to account well for the residual stress generation. Again, strong correlation between  $\langle k_{\parallel} \rangle$  (top-right) and  $\omega_E^{ZF}$  (midright) shown in Fig. 13 elucidates that the CTEM self-generated zonal flow shear plays a key role in breaking  $k_{\parallel}$  symmetry. It is interesting to compare the effect of equilibrium shear, which is included in this simulation via the radial force balance relation, and the effect of zonal flow shear. The total  $\mathbf{E} \times \mathbf{B}$  shear rate (zonal flows + equilibrium  $\mathbf{E} \times \mathbf{B}$  flow) is plotted in the bottom panel, showing very similar structures to those of pure zonal flows. This is because the equilibrium shear is much weaker than the zonal flows. In this particular case, the equilibrium shear is shown to have a minor effect on  $k_{\parallel}$  symmetry breaking and thus on residual stress generation. However, the equilibrium flow shear is expected to have

a significant effect on turbulence driven residual stress in regions of transport barriers,<sup>11</sup> both in the core and at the edge.

It has been remarked that the mechanism of turbulence intensity does not fully explain the residual generation, particularly in the outer core region ( $r/a \geq 0.55$ ). It has been suggested in theory that turbulence intensity gradients can also contribute to driving residual stress,<sup>12</sup> in addition to the turbulence intensity. The intensity gradients in both the radial direction and the wavenumber  $k_r$  direction may act for driving a residual stress. Here, we focus our discussion on the role of the intensity gradient in the radial direction. Figure 14 shows the spatiotemporal evolution of the quantity  $-\langle k_{\parallel} \rangle \Sigma \partial / \partial r (\delta \Phi^2)$ , which can be used to approximately represent the intensity gradient driven residual stress. Its apparent correlation with the directly calculated residual stress (top-left panel of Fig. 13) is noted particularly in the outer core region where a significant effect of the turbulence intensity is not observed. This simulation result is a clear identification of the turbulence intensity gradient driving residual stress in the presence of zonal flow shear induced symmetry breaking.

A few highly remarkable, interesting features revealed in the CTEM simulation are worth further discussion. First, the CTEM-driven residual stress changes sign from outward in the inner core region to inward in the outer core region, as is more clearly seen in Fig. 15 (upper-left panel), which shows the radial profile of the residual stress (time averaged over steady state). What determines the sign of the residual stress, particularly its relation with plasma parameters, remains as an important issue. The residual stress is shown to act as an intrinsic torque effectively. The resultant parallel flow (or toroidal flow) generation process is demonstrated in the lower panels of Fig. 15. In this case, a parallel flow is driven mostly in the counter- $\mathbf{B}$  direction in the whole region  $r/a \sim 0.25 - 0.8$  where CTEM turbulence is excited (see upper-right panel). The corresponding toroidal rotation is in the cocurrent direction for this DIII-D geometry case, which is in agreement with the experimental trend of intrinsic rotation observed in various tokamaks. The maximum parallel flow velocity generated at the end of the simulation reaches  $\sim 5\%$  of the local ion thermal velocity (see upper-right

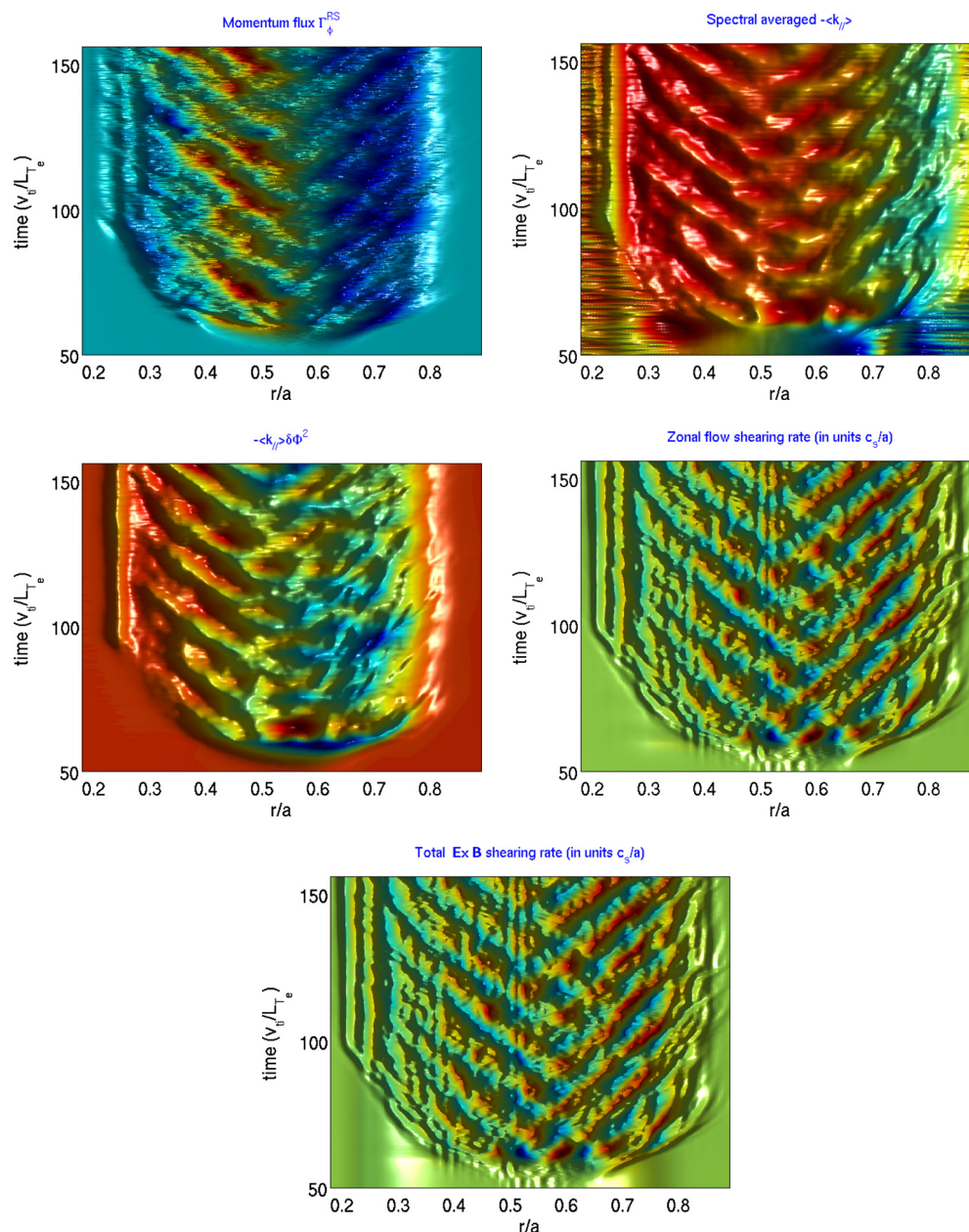


FIG. 13. (Color online) Spatiotemporal evolution of radial flux of toroidal momentum (top-left),  $\langle k_r \rangle \Sigma \delta\Phi_{mn}^2$  (midleft), spectrum-averaged  $\langle k_r \rangle$  (top-right), zonal flow shearing rate (midright), and total  $\mathbf{E} \times \mathbf{B}$  shearing rate (bottom) from simulation of CTEM turbulence.

panel). Further, the CTEM turbulence and transport are characterized by burstings, which emerge regularly in time and propagate radially (see Fig. 14). The coherent spatiotemporal bursting phenomenon was observed in ITG simulations<sup>7</sup> but appears more pronounced in the TEM turbulence regime. The bursting generation frequency and the radial propagation velocity are estimated to be  $f_b \sim 0.1c_s/a$  and  $V_b \sim (5-10) \times 10^{-3}c_s$ , respectively, where  $c_s$  is the sound speed. More interestingly, it is found that the temporal burstings and radial propagation are also directly displayed in the parallel flow during its generation process, as is clearly seen in the lower panels of Fig. 15. Particularly, it is shown that small parallel flow perturbations are generated locally (in the center of the plasma in the simulation case) by the turbulence and then propagate radially. The measured propagation ve-

locity is  $\sim 7 \times 10^{-3}c_s$ . This flow pinch phenomenon revealed in the simulations may have analogs in experiments. The radially inward propagation of toroidal flow perturbations generated by modulated beams in the peripheral region near the plasma edge was demonstrated in JT-60U experiments,<sup>16,37</sup> which was attributed to the turbulence driven momentum pinch. Nevertheless, our simulation results of flow pinch may offer a new insight into the underlying dynamics governing the radial penetration of localized modulated flows in perturbation experiments. We should particularly point out that the mesoscale phenomena and their critical role in determining plasma transport and its radially nonlocal nature are highly pronounced in the TEM turbulence regime.

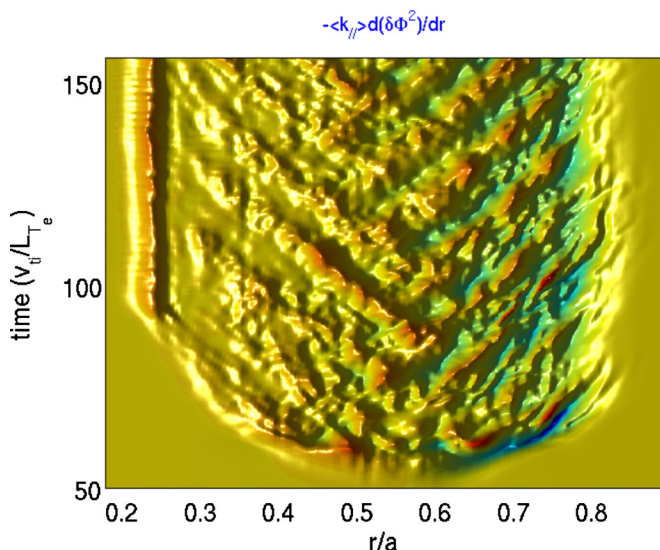


FIG. 14. (Color online) Spatiotemporal evolution of  $\langle k_{||} \rangle \Sigma \partial / \partial r (\delta \Phi^2)$ , which represents the part of the residual stress driven by the turbulence intensity gradient.

## VI. PHASE SPACE STRUCTURES OF TURBULENCE DRIVEN FLUXES

It is highly interesting and instructive to examine the phase space structures of various turbulence driven fluxes. This type of study can provide physical pictures at a very fundamental level with regard to which and how particles

contribute to plasma transport due to turbulence. Particularly, this can help elucidate the roles of resonant and nonresonant particles.

In Fig. 4, it is observed that the ITG driven toroidal momentum flux reverses its sign from inward in the post saturation phase to outward in the long-time steady state. The phase space structures of the momentum flux at the two stages are presented in Fig. 16. To be precise, illustrated in Fig. 16 is the function  $\Gamma_{\phi}(\mathbf{r}, v_{||}, v_{\perp})$ , which relates to the momentum flux [defined in Eq. (11) without a flux-surface average], defined by  $\Gamma_{\phi} = \int dv_{||} dv_{\perp} \Gamma_{\phi}(\mathbf{r}, v_{||}, v_{\perp})$ , and is calculated at the midplane ( $\theta=0$ ) and  $r/a=0.54$ . A similar definition applies to the particle and energy fluxes whose structures are also discussed in this section. First, it is observed that the momentum flux is carried mostly by passing and barely trapped ions. There are four signed peaks, which are regularly located in the  $(v_{||}, v_{\perp})$  space, indicating dominant contributions from four different particle groups. The four groups of particles are distinguished by the amplitude of energy (low or high) and the sign of  $v_{||}$  (positive or negative) and contribute to the momentum flux in different ways. Specifically, one higher energy group with positive  $v_{||}$  and one lower energy group with negative  $v_{||}$  make positive contributions to the momentum flux (i.e., outward momentum flux); another higher energy group with negative  $v_{||}$  and another lower energy group with positive  $v_{||}$  make negative contributions to the momentum flux (i.e., inward momentum flux). On the other hand, contributions from high energy ions with  $|v_{||}|, v_{\perp} > 3$  are small. Note that these characteristic phase

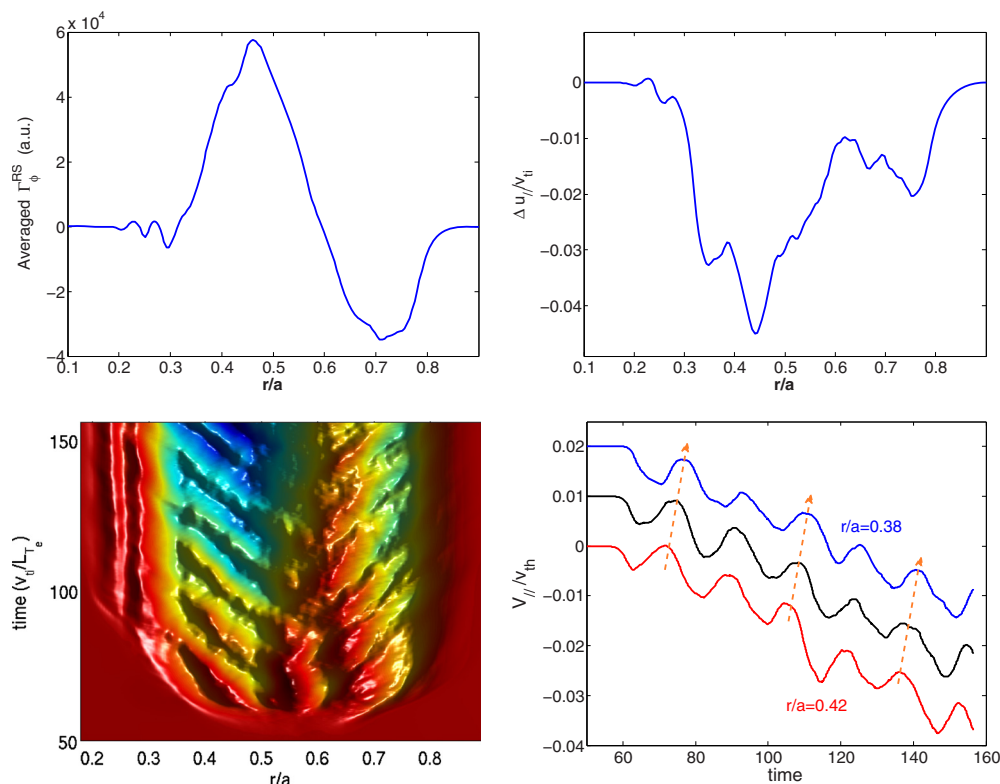


FIG. 15. (Color online) Averaged momentum flux (residual stress) at steady state vs minor radius (upper-left), radial profile of ion parallel flow (in counter-**B**, i.e., cocurrent direction) at end of simulation (up-right), spatiotemporal evolution of the parallel flow (lower-left), and time history of the parallel flow at three radial locations (lower-right), which more clearly illustrates flow pinch phenomenon.



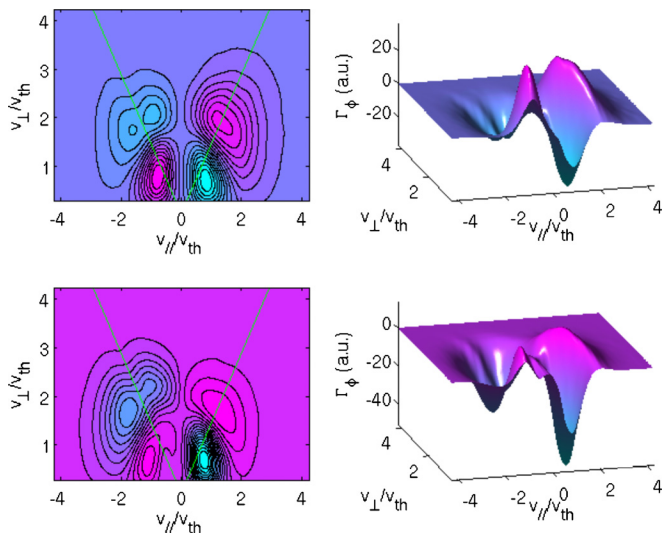


FIG. 16. (Color online) Phase space dependence of ITG turbulence driven on toroidal momentum flux at long-time steady state phase (top) and at post saturation phase (bottom), corresponding to Fig. 4. The straight lines denote the boundaries of trapping-passing particles.

space structures persistently appear in both the postsaturation stage and the long-time steady state with no considerable difference, while the net momentum fluxes at the two stages are in opposite directions. As for what makes the total momentum flux inward or outward, the simulation results suggest that it depends on the relative amount of each particle group's contribution, which may have to do with the details of the turbulence spectrum.

It is highly instructive to compare phase space structures in different transport channels. As illustrated in Fig. 17, the ITG driven heat flux is carried by different ions in a different way. First, the heat flux is carried mostly by trapped and barely trapped ions. Higher energy, mostly trapped, ions make the largest contribution, which is positive and peaked at  $v \sim 2.5v_{th}$ ; lower energy ions around trapped-passing boundaries centered at  $v \sim 1v_{th}$  make a negative contribution. These features share similarity to some extent with the neo-classical transport in the collisionless regime, which may imply that the ion transport driven by the fluid-type ITG turbulence is nonresonance dominated.

We have shown in Sec. V that the trapped electron physics has a strong impact on ITG turbulence, particularly in a regime close to or below the ITG marginality. Particularly, the nonadiabatic electrons are shown to substantially en-

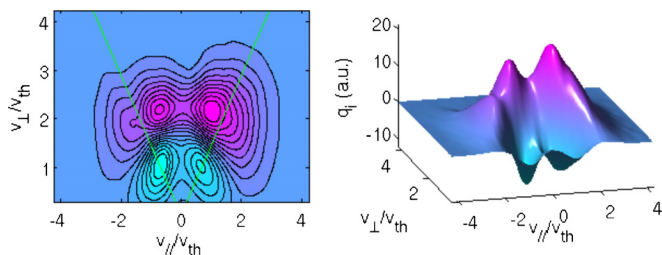


FIG. 17. (Color online) Phase space dependence of ITG turbulence driven ion heat flux at the steady state, corresponding to Fig. 4.

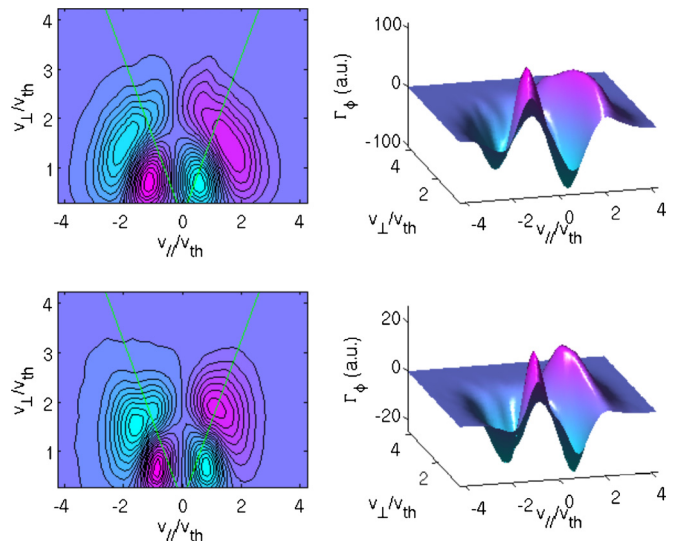


FIG. 18. (Color online) Phase space structures of toroidal momentum flux driven by ITG turbulence with kinetic electrons (top) and adiabatic electrons (bottom). This is from the same simulation of Fig. 11.

hance residual stress generation. It is interesting to understand how the inclusion of trapped electrons could change the way of ions interacting with turbulence and thus carrying the momentum flux. The phase space dependence of the momentum flux is compared between the ITG turbulence with adiabatic and nonadiabatic electrons in Fig. 18, which is obtained from the same simulation of the DIII-D discharge as in Fig. 11. It is shown that the ITG driven momentum flux in experimental conditions possesses all the characteristics described previously for Fig. 16 for the case of large aspect ratio circular geometry and model plasma profiles. More importantly, trapped electrons are found not to change the qualitative phase space structure of ITG driven momentum and heat fluxes. The enhancement in the momentum flux production due to trapped electrons in ITG turbulence is mainly related to the increase of turbulence intensity.

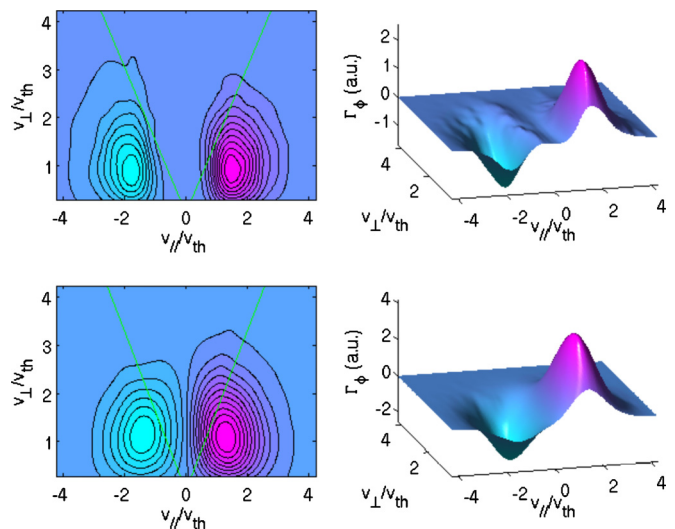


FIG. 19. (Color online) Phase space structures of momentum flux in  $\nabla T_e$ -driven (top) and  $\nabla n$ -driven (bottom) CTEM turbulence.

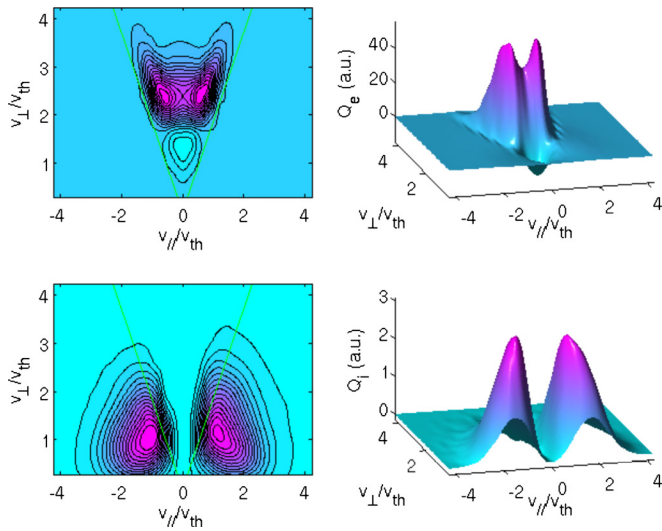


FIG. 20. (Color online) Phase space structures of electron (top) and ion (bottom) energy flux in CTEM turbulence.

For typical plasma parameters of fusion experiments, collisionless TEM turbulence can be a major source to drive multiple-channel transport. Now we turn to discuss the phase space characteristics of plasma transport produced by CTEM turbulence. First, the TEM turbulence driven momentum flux shows highly distinct topology in phase space structures compared to that of ITG turbulence. Figure 19 shows the CTEM simulation results of the residual stress component. For both  $\nabla T_e$ - and  $\nabla n$ -driven CTEM turbulence, the ion momentum flux of residual stress is carried by two groups of ions, which are divided by the sign of  $v_{\parallel}$ : ions with positive  $v_{\parallel}$  carry outward flux and ions with negative  $v_{\parallel}$  carry inward flux. The dominant contributions come from passing ions at around  $v_{\perp}/v_{th} \sim 1$  and  $v_{\parallel}/v_{th} \sim \pm(1.5-2)$ . While the phase

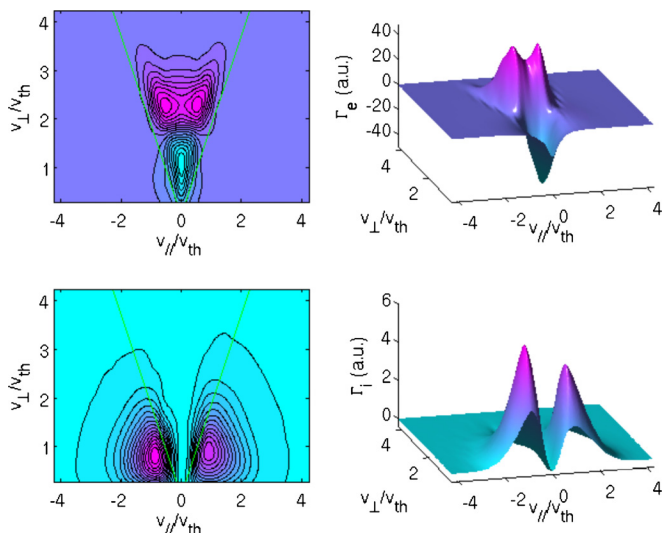


FIG. 21. (Color online) Phase space structures of electron (top) and ion (bottom) particle flux in CTEM turbulence. This is obtained from the same simulation in Fig. 21.

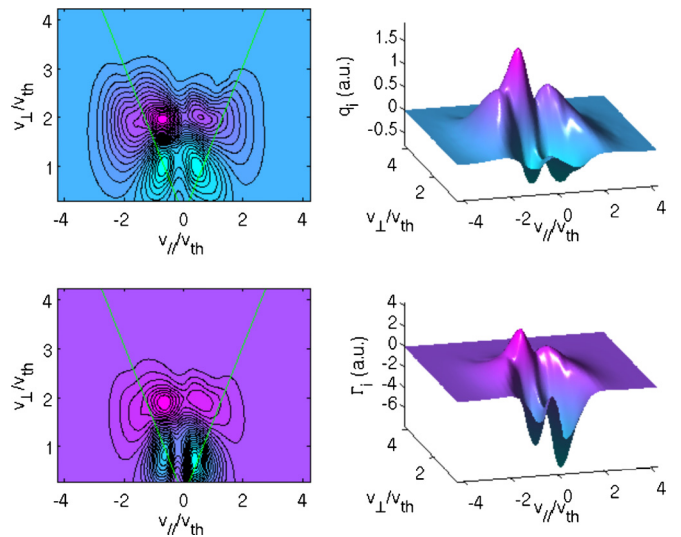


FIG. 22. (Color online) Phase space structures of heat flux (top) and particle flux (bottom) in ITG turbulence with adiabatic electrons.

space structures between the  $\nabla T_e$ - and  $\nabla n$ -driven cases look qualitatively similar, it is also possible to notice a subtle difference, i.e., in  $\nabla T_e$ -driven CTEM turbulence, the trapped ion region is basically a null region for the momentum flux.

Compared to the ITG case, the CTEM turbulence driven ion energy transport is also caused by ions from different regions and in a different way. As shown in the lower panel of Fig. 20, the dominant contributions come from two groups of passing ions, both carrying positive (outward) ion flux. On the other hand, the electron responses in CTEM turbulence are shown to concentrate sharply in the trapped region, clearly spelling out the effect of trapped electron modes. As illustrated in the upper panel of Fig. 20, an outward flux of energy is carried by trapped electrons with higher energy, with little contribution from passing electrons. At the same time, deeply trapped, low energy electrons are shown to carry an inward but small flux for energy. Moreover, the electron phase space structures appear symmetric around  $v_{\parallel}=0$ . Apparently, the electron transport is dominated by the precession drift resonance of trapped electrons.

Remarkably, our simulation results clearly reveal that the particle flux is carried by the same particles in the phase space as the energy flux. This result holds true for both ions and electrons at different turbulence regimes. The results of CTEM driven ion and electron flux are presented in Fig. 21, which displays high similarity to the energy fluxes in Fig. 20. In the regime of ITG turbulence with adiabatic electrons, Fig. 22 illustrates how a net outward heat flux and a vanishing ion particle flux can be produced by the same groups of ions. Higher energy ions, mostly trapped ones, carry outward fluxes for both heat and particle, and lower energy ions, mostly barely trapped ones, carry inward fluxes for both heat and particle. For the heat flux, the inward flux is greater than the outward, and a net outward flux remains. For the particle flux, however, the inward and outward components are balanced with each other, resulting in a vanishing net flux.

## VII. CONCLUSIONS

Global gyrokinetic simulations using experimentally relevant parameters have revealed an important nonlinear flow generation process due to the residual stress produced by electrostatic turbulence of ion temperature gradient modes and trapped electron modes. Turbulence self-generated low frequency zonal flow shear has been identified to be a key universal mechanism in various turbulence regimes for  $k_{\parallel}$  symmetry breaking, which is a critical ingredient for parallel (and toroidal) flow generation by turbulence. The principle results of this study are summarized as follows.

- (i) The nonlinear residual generation has been clearly observed, for the first time, in CTEM turbulence. Particularly, in addition to turbulence fluctuation intensity driving residual stress, which was also reported previously for ITG turbulence,<sup>26</sup> the intensity gradient is also identified to drive significant residual stress by acting with the CTEM self-generated zonal flow shear, which induces symmetry breaking in the  $k_{\parallel}$  spectrum.
- (ii) The residual stress, acting as an intrinsic torque, is shown to spin up toroidal rotation effectively. In the simulated CTEM case with typical DIII-D parameters, where the plasma is initially rotation-free and momentum-source-free, a net toroidal rotation is produced in the cocurrent direction in the whole turbulence region. This is consistent with the experimental trend of observed intrinsic rotation. The total toroidal momentum is generated at an approximately constant rate, with the peak of the corresponding parallel flow profile at the end of the simulation reaching  $\sim 5\%$  of local ion thermal velocity. This net directional mechanical flow generation phenomenon is an indication of momentum transfer from turbulence waves to particles via residual stress.
- (iii) The CTEM turbulence and transport including the momentum flux are characterized by burstings, which emerge regularly in time and propagate radially both inward and outward. The mesoscale phenomena appear more pronounced than in the ITG turbulence regime and are found to play a critical role in determining plasma transport and its radially nonlocal nature. One highly remarkable result is the observation of the flow pinch phenomenon. Specifically, toroidal flow perturbations, which are generated locally (in the center of the plasma in the simulation case) by the turbulence, are found to propagate radially. This result may offer an interesting new insight into the experimental phenomenon of radially inward penetration of perturbed flows created by modulated beams in peripheral regions.
- (iv) In the ITG turbulence regime, the intrinsic torque associated with residual stress is predicted to increase close to linearly with the value of the temperature gradient offset from the ITG critical gradient,  $(R_0/L_{T_i} - R_0/L_{T_i}^{\text{crit}})$ . The dominant underlying physics governing this scaling is that both the residual stress and the zonal flow shear are increased with the turbu-

lence intensity, which, in turn, is increased with the strength of the ITG drive  $R_0/L_{T_i}$ . This simulation result is in qualitative agreement with experimental trends observed in various devices, such as the Rice scaling,<sup>36</sup> in which the increment of central toroidal flow velocity for H-mode plasmas scales linearly with the increment in the plasma stored energy divided by the plasma current.

- (v) For typical tokamak parameters, the nonlinearly generated residual stress is found to contribute up to more than 50% of the total momentum flux produced by ITG turbulence. It is plausible that the portion of the residual stress is shown to increase with the decrease of the rotation gradient. The intrinsic Prandtl number is shown to increase with the ion temperature gradient, specifically, ranging from  $P_r \sim 0.4$  to  $0.7$  for  $R_0/L_{T_i} \sim 5.5$ – $8.5$ . This result is in general agreement with observations in NSTX where the estimated intrinsic Prandtl number  $P_r \sim 0.5$ – $0.8$  was reported from the experimental database of various shots.<sup>41</sup>
- (vi) While the critical effect of zonal flow shear on the parallel wavenumber spectrum is clarified, our simulations, particularly with electron physics included, also indicate the existence of other mechanisms beyond  $\mathbf{E} \times \mathbf{B}$  shear for symmetry breaking. The possible mechanisms include the effects of magnetic shear, nonlinear mode couplings, and turbulent radial current, which will be addressed in a future publication.
- (vii) Our simulations reveal highly distinct phase space structures between ITG and TEM turbulence for momentum, energy and particle fluxes, with a lot of interesting details with regard to which and how particles contribute to ion and electron transport in different channels. This study can ultimately help elucidate the roles of resonant and nonresonant particles in plasma transport in different turbulence regimes, which is a highly nontrivial issue under turbulence circumstances with many modes nonlinearly coupled together.
- (viii) In the ITG marginality regime, trapped electron physics is shown to play a critical role in determining plasma transport, not only producing the proper ion heat flux in experiments but also largely enhancing the residual stress generation. However, trapped electrons do not change the qualitative phase space structure of ITG driven momentum and heat fluxes.

## ACKNOWLEDGMENTS

We would like to acknowledge useful discussions with Dr. F. L. Hinton, Dr. S. M. Kaye, Dr. J. Lang, Dr. W. W. Lee, Dr. C. J. McDevitt, and Dr. W. Solomon. This work was supported by U.S. DOE under Contract No. DE-AC02-09CH11466 and the SciDAC project for Gyrokinetic Particle Simulation of Turbulent Transport in Burning Plasmas. Simulations were performed at the National Energy Research Scientific Computing Center (NERSC) and the National Center for Computational Sciences (NCCS).

- <sup>1</sup>F. L. Hinton and S. K. Wong, *Phys. Fluids* **28**, 3082 (1985).
- <sup>2</sup>J. E. Rice, W. D. Lee, E. S. Marmor, P. T. Bonoli, R. S. Granetz, M. J. Greenwald, A. E. Hubbard, I. H. Hutchinson, J. H. Irby, Y. Lin, D. Mossessian, J. A. Snipes, S. M. Wolfe, and S. J. Wukitch, *Nucl. Fusion* **44**, 379 (2004).
- <sup>3</sup>J. S. deGrassie, J. E. Rice, K. H. Burrell, R. J. Groebner, and W. M. Solomon, *Phys. Plasmas* **14**, 056115 (2007).
- <sup>4</sup>L.-G. Eriksson, T. Hellsten, M. F. F. Nave, J. Brzozowski, K. Holmstrom, T. Johnson, J. Ongena, K.-D. Zastrow, and J.-E. Contributors, *Plasma Phys. Controlled Fusion* **51**, 044008 (2009).
- <sup>5</sup>N. Mattor and P. H. Diamond, *Phys. Fluids* **31**, 1180 (1988).
- <sup>6</sup>S. D. Scott, P. H. Diamond, R. J. Fonck, R. J. Goldston, R. B. Howell, K. P. Jaehnig, G. Schilling, E. J. Synakowski, M. C. Zarnstorff, C. E. Bush, E. Fredrickson, K. W. Hill, A. C. Janos, D. K. Mansfield, D. K. Owens, H. Park, G. Pautasso, A. T. Ramsey, J. Schivell, G. D. Tait, W. M. Tang, and G. Taylor, *Phys. Rev. Lett.* **64**, 531 (1990).
- <sup>7</sup>W. X. Wang, T. S. Hahm, S. Ethier, G. Rewoldt, W. W. Lee, W. M. Tang, S. M. Kaye, and P. H. Diamond, *Proceedings of the 22nd IAEA Fusion Energy Conference*, Geneva, Switzerland (IAEA, Vienna, 2008), IAEA-CN-165/TH-P8-44.
- <sup>8</sup>P. H. Diamond, C. J. McDevitt, O. D. Gurcan, T. S. Hahm, W. X. Wang, E. S. Yoon, I. Holod, Z. Lin, V. Naulin, and R. Singh, *Nucl. Fusion* **49**, 045002 (2009).
- <sup>9</sup>C. J. McDevitt, P. H. Diamond, O. D. Gurcan, and T. S. Hahm, *Phys. Plasmas* **16**, 052302 (2009).
- <sup>10</sup>R. Dominguez and G. M. Staebler, *Phys. Fluids B* **5**, 3876 (1993).
- <sup>11</sup>Ö. D. Gürçan, P. H. Diamond, T. S. Hahm, and R. Singh, *Phys. Plasmas* **14**, 042306 (2007).
- <sup>12</sup>P. H. Diamond, C. J. McDevitt, O. D. Gurcan, T. S. Hahm, and V. Naulin, *Phys. Plasmas* **15**, 012303 (2008).
- <sup>13</sup>C. J. McDevitt, P. H. Diamond, O. D. Gurcan, and T. S. Hahm, *Phys. Rev. Lett.* **103**, 205003 (2009).
- <sup>14</sup>J. Weiland, R. Singh, H. Nordman, P. Kaw, A. G. Peeters, and D. Strinzi, *Nucl. Fusion* **49**, 065033 (2009).
- <sup>15</sup>Y. Camenen, A. G. Peeters, C. Angioni, F. J. Casson, W. A. Hornsby, A. P. Snodin, and D. Strintzi, *Phys. Rev. Lett.* **102**, 125001 (2009).
- <sup>16</sup>M. Yoshida, Y. Koide, H. Takenaga, H. Urano, N. Oyama, K. Kamiya, Y. Sakamoto, K. Kamada, and JT-60 Team, *Plasma Phys. Controlled Fusion* **48**, 1673 (2006).
- <sup>17</sup>W. X. Wang, Z. Lin, W. M. Tang, W. W. Lee, S. Ethier, J. L. V. Lewandowski, G. Rewoldt, T. S. Hahm, and J. Manickam, *Phys. Plasmas* **13**, 092505 (2006).
- <sup>18</sup>R. J. Goldston, "Basic Physical Processes of Toroidal Fusion Plasmas," in *Proceedings of Course and Workshop*, Varenna, edited by G. P. Lampis, M. Lontano, G. G. Leotta, A. Malein, and E. Sindoni (Monotypia Franchi, Citta di Castello, Italy, 1985), Vol. 1, p. 165.
- <sup>19</sup>W. X. Wang, G. Rewoldt, W. M. Tang, F. L. Hinton, J. Manickam, L. E. Zakharov, R. B. White, and S. Kaye, *Phys. Plasmas* **13**, 082501 (2006).
- <sup>20</sup>I. Manuilskiy and W. W. Lee, *Phys. Plasmas* **7**, 1381 (2000).
- <sup>21</sup>G. Rewoldt, W. M. Tang, and M. S. Chance, *Phys. Fluids* **25**, 480 (1982).
- <sup>22</sup>X. Lapillonne, S. Brunner, T. Dannert, S. Jolliet, A. Marinoni, L. Villard, T. Grler, F. Jenko, and F. Merz, *Phys. Plasmas* **16**, 032308 (2009).
- <sup>23</sup>Y. Chen and S. Parker, *J. Comput. Phys.* **189**, 463 (2003).
- <sup>24</sup>W. X. Wang, T. S. Hahm, P. H. Diamond, S. Ethier, W. M. Tang, W. W. Lee, G. Rewoldt, W. Solomon, S. M. Kaye, J. Lang, and R. Kolesnikov, *Bull. Am. Phys. Soc.* **54**(15), 327 (2009).
- <sup>25</sup>W. X. Wang, T. S. Hahm, W. W. Lee, G. Rewoldt, J. Manickam, and W. M. Tang, *Phys. Plasmas* **14**, 072306 (2007).
- <sup>26</sup>W. X. Wang, T. S. Hahm, S. Ethier, G. Rewoldt, W. Lee, W. M. Tang, S. M. Kaye, and P. H. Diamond, *Phys. Rev. Lett.* **102**, 035005 (2009).
- <sup>27</sup>D. Strintzi, A. G. Peeters, and J. Weiland, *Phys. Plasmas* **15**, 044502 (2008).
- <sup>28</sup>P. H. Diamond, V. B. Lebedev, Y. M. Liang, A. V. Gruzinov, I. Gruzinova, and M. Medvedev, *Proceedings of the 15th IAEA Fusion Energy Conference*, Seville, Spain (IAEA, Vienna, 1994), IAEA-CN-60/D2II6.
- <sup>29</sup>X. Garbet, Y. Sarazin, P. Ghendrih, S. Benkadda, P. Beyer, C. Figarella, and I. Voitsekhovitch, *Phys. Plasmas* **9**, 3893 (2002).
- <sup>30</sup>F. J. Casson, A. G. Peeters, Y. Camenen, W. A. Hornsby, A. P. Snodin, D. Strintzi, and G. Szepesi, *Phys. Plasmas* **16**, 092303 (2009).
- <sup>31</sup>T. S. Hahm, P. H. Diamond, O. D. Gurcan, and G. Rewoldt, *Phys. Plasmas* **14**, 072302 (2007).
- <sup>32</sup>E. S. Yoon and T. S. Hahm, *Nucl. Fusion* **50**, 064006 (2010).
- <sup>33</sup>G. R. Tynan, P. H. Diamond, O. Gurcan, C. Holland, S. H. Muller, M. Xu, Z. Yan, J. Yu, P. Manz, M. Ramisch, U. Stroth, Y. Nagashima, S. I. Itoh, M. Yagi, S. Inagaki, A. Fujisawa, N. Kasuya, K. Itoh, T. Windisch, O. Grulke, and T. Klinger, *Proceedings of the 22nd IAEA Fusion Energy Conference*, Geneva, Switzerland (IAEA, Vienna, 2008), IAEA-CN-165/EX-P5-40.
- <sup>34</sup>T. S. Hahm and K. H. Burrell, *Phys. Plasmas* **2**, 1648 (1995).
- <sup>35</sup>W. M. Solomon, K. H. Burrell, J. S. deGrassie, R. Budny, R. J. Groebner, J. E. Kinsey, G. J. Kramer, T. C. Luce, M. A. Makowski, D. Mikkelsen, R. Nazikian, C. C. Petty, P. A. Politzer, S. D. Scott, M. A. Van Zeeland, and M. C. Zarnstorff, *Plasma Phys. Controlled Fusion* **49**, B313 (2007).
- <sup>36</sup>J. E. Rice, A. Ince-Cushman, J. S. deGrassie, L.-G. Eriksson, Y. Sakamoto, A. Scarabosio, A. Bortolon, K. H. Burrell, B. P. Duval, C. Fenzi-Bonizec, M. J. Greenwald, R. J. Groebner, G. T. Hoang, Y. Koide, E. S. Marmor, A. Pochelon, and Y. Podpaly, *Nucl. Fusion* **47**, 1618 (2007).
- <sup>37</sup>M. Yoshida, Y. Kamada, H. Takenaga, Y. Sakamoto, H. Urano, N. Oyama, G. Matsunaga, and JT-60 Team, *Phys. Rev. Lett.* **100**, 105002 (2008).
- <sup>38</sup>J. E. Rice, *Bull. Am. Phys. Soc.* **54**(15), 21 (2009).
- <sup>39</sup>K. Ida, M. Yoshinuma, K. Nagaoka, M. Osakabe, S. Morita, M. Goto, M. Yokoyama, H. Funaba, S. Murakami, K. Ikeda, H. Nakano, K. Tsumori, Y. Takeiri, O. Kaneko, and LHD experimental group, *Nucl. Fusion* **50**, 064007 (2010).
- <sup>40</sup>L. Wang and T. S. Hahm, *Phys. Plasmas* **16**, 082302 (2009).
- <sup>41</sup>S. M. Kaye, W. Solomon, R. E. Bell, B. P. LeBlanc, F. Levinton, J. Menard, G. Rewoldt, S. Sabbagh, W. Wang, and H. Yuh, *Nucl. Fusion* **49**, 045010 (2009).